UQAC
Université du Québec
à Chicoutimi

Quench Sensitivity of High Pressure Vacuum Die Castings and Permanent Mold Castings of Aural-3/5 Alloys

By

Mengyun Liu

Master Candidate: Mengyun Liu

Permanent code: LIUM03529309

Director: Prof. X.Grant Chen

Co-director: Prof. Zhan Zhang

Québec, Canada

Abstract

The quench sensitivities of Al-10wt%Si-0.5wt%Mg alloy (Aural^{TM}-3) in permanent mold (PM) and high pressure vacuum die (HPVD) castings as well as the quench sensitivity of Al-7wt%Si-0.2wt%Mg alloy (Aural^{TM}-5) in HPVD have been investigated by time-temperature-transformation (TTT) and time-temperature-property (TTP) curves using an interrupted quench technique. The sensitivity temperature range of Aural^{TM}- 3 HPVD is from 275 ºC to 450 ºC, and its nose temperature is 375ºC, while the nose temperature of Aural^{TM}- 3 PM is 350 ºC and its sensitivity temperature range is from 255 ºC to 430 ºC. The nose temperature of Aural^{TM} 5 HPVD is 350 ºC and its quench sensitivity temperature range is from 260 to 430 ºC. The mechanical properties of the alloys with various cooling rates were predicted using quench factor analysis method. For Aural^{TM}-3 HPVD, the cooling rate should be higher than 20 ºC/s to obtain more than 95% of the hardness on T6 condition, which is 17 ºC/s for Aural^{TM}-3 PM and 6 ºC/s for Aural^{TM} 5 HPVD. Different types of Mg_2Si particles precipitated from supersaturated aluminum matrix during isothermal holding at various temperature. At nose temperature, coarse Mg_2Si particles mainly precipitated along grain boundaries in HPVD samples, and however, in PM samples, rod-like Mg_2Si precipitates were observed nucleating on Mn-containing dispersoids in aluminum grains. The temperatures of β'- Mg_2Si and β- Mg_2Si particles precipitated from supersaturated aluminum matrix in Aural^{TM}-3 HPVD are lower than those in Aural^{TM}-3 PM according to the results of differential scanning

calorimetry (DSC) analysis. The phase transformation kinetics of Aural^{TM}-5 HPVD during isothermal holding have been discussed. Aural^{TM}-3 HPVD has higher quench sensitivity than Aural^{TM}-3 PM and Aural^{TM}-5 HPVD.

The difference of quench sensitivity between Aural^{TM}-3 HPVD and PM is mainly due to the microstructure variation of both castings. HPVD provided much finer microstructure than PM due to rapid injection speed of liquid metal and high pressure. Fine microstructure in HPVD comes along with a large amount of grain boundaries, which act as nucleation sites and greatly reduced the nucleation energy required for precipitation during insufficient quenching. On the other hand, PM casting has a relatively larger amount of dispersoids, which are in aid of precipitation during insufficient quenching. The TTP/TTT and DSC results showed that the effect of grain boundaries in HPVD is larger than dispersoids in PM, which leads to higher quench sensitivity in Aural^{TM}-3 HPVD.

As for Aural^{TM}-5 and Aural^{TM}-3 HPVD, the difference of their quench sensitivity is caused by the concentration of alloying elements. Aural^{TM}-5 has lower concentrations of Si and Mg that markedly reduced the driving force of precipitation. On the other hand, the larger grain size in Aural^{TM}-5 diminished the grain boundary precipitation. Thus, the quench sensitivity of Aural^{TM}-5 is lower than Aural^{TM}-3.

Résumé

La sensibilité à la trempe du moule permanent (PM) Al-10wt%Si-0.5wt%Mg (Aural^{TM}-3) et du moulage sous vide à haute pression (HPVD) and Al-7wt%Si-0.2wt%Mg (Aural^{TM}-5) HPVD ont été étudiés par des courbes de temps-température-transformation (TTT) et de temps-température-propriété (TTP) en utilisant une technique de trempe interrompue. La plage de température de sensibilité de l'Aural^{TM}-3 HPVD se situe entre 275 ºC et 450 ºC et la température du nez est de 375 ºC, tandis que la température du nez des moules permanents est de 350 ºC et la plage de sensibilité de 255 ºC à 430 ºC. La température du nez de l'Aural^{TM} 5 HPVD est de 350ºC. Sa plage de température de trempe est de 260-430ºC. Les propriétés mécaniques des pièces coulées avec différentes vitesses de refroidissement ont été prédites en utilisant une méthode d'analyse par facteur de trempe. Pour le HPVD Aural^{TM}-3, la vitesse de refroidissement serait supérieure à 20 ºC/s pour obtenir plus de 95% de la dureté à l'état T6, soit 17 ºC/s pour l'Aural^{TM}-3 PM et 6 ºC/s pour l'Aural^{TM} 5 HPVD. Différents types de particules de Mg_2Si précipitent à partir de la matrice d'aluminium sursaturée au cours de la tenue isotherme à différentes températures. À la température du nez, les particules grossières de Mg_2Si précipitent principalement le long des joints de grains dans les échantillons de HPVD. Cependant, pour les moules permanents, des précipités de Mg_2Si en forme de bâtonnets ont été observés dans des grains d'aluminium. Les températures des particules β 'et β précipitées à partir de la matrice d'aluminium sursaturée dans l'Aural^{TM}-3 HPVD sont inférieures à celles de l'Aural^{TM}-3 （PM） selon

l'analyse par calorimétrie différentielle à balayage (DSC). La cinétique de transformation de phase du HPVD Aural^{TM}-5 au cours de la tenue isotherme a été discutée. Aural^{TM}-3 HPVD a une sensibilité à la trempe plus élevée que l'Aural^{TM}-3 PM et l'Aural^{TM}-5 HPVD.

La différence de sensibilité à la trempe entre l'Aural^{TM}-3 HPVD et les moules permanents est principalement due à la divergence de la microstructure des pièces moulées. HPVD a fourni une microstructure beaucoup plus fine que les particules en raison de la vitesse d'injection rapide du métal liquide et de la haute pression. La microstructure fine s'accompagne d'une grande quantité de joints de grains. Il agirait comme des sites de nucléation et réduirait considérablement l'énergie de nucléation nécessaire à la précipitation lors d'une trempe insuffisante. Par ailleurs, les particules ont une quantité relativement plus grande de dispersoïdes qui aideraient à précipiter lors d'une trempe insuffisante. Mais les résultats du TTP / TTT et du DSC ont montré que l'effet des joints de grains dans le HPVD est plus important que celui des dispersoïdes dans les moules permanents, ce qui conduit à une sensibilité accrue à la trempe dans le HPVD Aural^{TM}-3.

En ce qui concerne l'Aural^{TM}-5 et l'Aural^{TM}-3 HPVD, la différence de sensibilité à la trempe est due à la concentration des éléments précipités. Aural^{TM}-5 a une concentration plus faible de Si et de Mg, ce qui réduit nettement la force motrice des précipitations. D’un autre côté, la plus grande taille de grain dans l'Aural^{TM}-5 a diminué la précipitation des joints de grains. Ainsi, la

sensibilité à la trempe d'Aural^{TM}-5 est beaucoup plus faible que celle d'Aural^{TM}-3.

Acknowledgement

First and foremost, it is with immense gratitude that I acknowledge the support and help of my two directors Prof. X Grant Chen and Prof. Zhan Zhang. Prof. Chen always gives me valuable and constructive suggestions during the planning and development of this research work. Prof. Zhang also offered functional guidance and timely help in my study. Without their help, I wouldn't be able to fulfill my goal of completing a master's degree successfully.

I am indebted to my many colleagues who supported me. They made my oversea studying much more fun and easier. Those includes Chen Li, Wei Xu, Sinan Chen, Xiaoming Qian, Xingli Chen, Zhixing Chen, Shuai Wang, Dong Li, Anil Arici.

In addition, I would like to express my profound gratitude to my host family parents Jean Jacques Reigneau and Catherine Lamontagne. They have given me so much supports and encouragements and make me feel like home. Heartfelt thanks to my friend Tony Murphy for helping me to correct grammatic problems and polish the sentences in my thesis.

Finally, but by no means least, I cannot find words to express my gratitude to my family whose love and guidance are with me in whatever I pursue. I also thank my partner Yan Côté for the unceasing encouragement, support and attention.

This project was financially supported by Natural Science and Engineering Research Council of Canada (NSERC) and Rio Tinto Aluminum through the NSERC Industry Research Chair in the Metallurgy of Aluminum

Transformation at Université du Québec à Chicoutimi (UQAC). I would like to thank both organizations for their support for my research.

Contents

List of figures

Chapter 2

Chapter 3

Chapter 4

List of tables

Chapter 2

Chapter 3

Chapter 4

Chapter 1 Introduction

1.1 Introduction

Aural™ alloys as one group of the Al-Si foundry alloys have a superior chemistry that offer a good balance of strength and ductility, while exhibiting excellent corrosion resistance without coating. Due to their very good fluidity, these alloys are well suited to the casting of thin and large structural components[1].

The casting process is one of the key factors that affect microstructure and ultimately affect mechanical properties. Al-Si alloys are widely applied to high pressure vacuum die (HPVD) casting and permanent mold (PM) casting. In HPVD, molten metal is injected into a cavity at high speeds (30-50 m/s in the gate velocity for aluminum alloys), which allow to solidify under high pressures (up to 200 MPa in the cavity) and with a high cooling rate (up to ~10^3 Ks^{-1})[2, 3]. The presence of vacuum in the die cavity generally reduces the casting flaws such as gas pores or shrinkage, allowing the application of heat treatment.

In the permanent mold (PM) casting, molten metal is poured into a metal mold under gravity with low speed (< 1.5 m/s in the gate for aluminum alloys) and solidified under low cooling rate (<10 Ks^{-1} for aluminum alloys)[4, 5]. Permanent mold casting generally avoids porosity and blister, which results in desirable grain structures that have high strength and soundness and are a good candidate for heat treatment.

The chemical composition is another key factor that affects mechanical properties. In Aural™ alloys, Mg and Si concentration have a great impact on the mechanical properties. Mg can associate with Si and form the compound

Mg_2Si phase during heat treatment. Needle-like β"- Mg_2Si is hardening phase which would greatly improve the mechanical properties after aging. Metastable states such as β"- Mg_2Si are typically silicon enriched. Having an excess of Si will meet the requirement of free energy thus predominance the metastable states and increase the mechanical properties. However, the presence of large, brittle, acicular flakes and plates of eutectic silicon leads to a substantial reduction of strength and elongation of the castings[6, 7]. Moreover, the increase in silicon content will increase the eutectic fraction which is distributed throughout the microstructure, thus providing a deleterious effect upon the electrochemical corrosion resistance[8]. Studies[9, 10] showed that with the increase of Mg concentration, the mechanical properties would increase. However, Mg enrichment will promote the formation of the β-Mg_2Si equilibrium phase[11]. Some studies[9, 12] also indicated that excessive addition of Mg would also decreases the ductility and fracture toughness of the materials. Therefore, the enrichment of certain phases or states with either Mg or Si must be considered in order to properly balance the alloy.

The ability to form a non-hardenable phase during quenching is called quench sensitivity[13]. Quench factor analysis (QFA), introduced by Evancho and Staley[14] in the 1970s, is an effective way to study quench sensitivity. It indicates that precipitation rate is an explicit function of temperature and the amount of solute remaining in solution[15]. Many studies[14-17] have associated QFA with C curves such as time-temperature-property (TTP) and time-temperature-transformation (TTT) curves to obtain important information such as the critical

time or nose temperature for precipitation during quenching, which can be used to predict the mechanical properties. Interrupted quenching techniques, in which a series of isothermal heating tests followed by quench are performed, have been widely used in determining C curves[14]. After mathematical calculations, isothermal C curves can be used to investigate continuous cooling processes[14].

1.2 Definition of problems

C curves studies initially started in wrought alloys, and gradually developed to casting alloys. Murat and Ralph[18] constructed TTP curves based on yield strength for D357 (Al-7Si-0.62Mg) alloy with unknown casting process, they reported that D357 is slightly less quench sensitive than 6061(Al-0.65Si-0.89Mg) and more quench sensitive than 6082(Al-0.92Si-0.59Mg), they thought the difference was caused by the Mg and Si concentration. Zhang and Zheng[19] studied the quench sensitivity of Al-7 pct Si- 0.4 pct Mg (A356) permanent mold (PM) casting alloy and compared it to 6063 wrought (Al-0.6 pct Mg-0.4 pct Si) alloy. They reported that excessive Si content would act as nucleation sites and increase quench sensitivity. Except for solute concentration, non-equilibrium defects such as excess vacancies, dislocations, grain boundaries and inclusions will act as nucleation sites and affect quench sensitivity. Ives, et al.[16] studied AA2024 alloy by constructing TTP curves. They revealed initial precipitation occurred at the grain boundary, followed by further precipitation at dispersoids. Subsequent transformation from non-equilibrium phase to equilibrium phase was the dominant factor. Casting process has a great impact on microstructure,

as well as the formation of non-equilibrium defects. Chemical composition also has a huge influence on mechanical properties. However, very few studies showed the impact of casting process on the quench sensitivity and very few studies investigated the effect of chemical composition on the HPVD casting alloys. Investigating the impact of the casting processes on non-equilibrium defects and the impact of chemical compositions will help us better understand the quench sensitivity and kinetic of precipitation.

1.3 Objectives

The main objective of the present work is on investigation of quench sensitivity and microstructure characterization of both Aural^{TM}-3 and 5 alloys by high pressure vacuum die casting and permanent mold casting. To achieve the objective, several research works will be carried out as follows:

1. To demonstrate the effect of casting processes (HPVD vs PM) on quench sensitivity;

2. To investigate the effect of different chemical compositions (Aural^{TM}-3 vs Aural^{TM}-5) on quench sensitivity;

3. To determine the effect of cooling rates on mechanical properties;

4. To characterize microstructure to assist in understanding the precipitation behaviour during quenching.

1.4 Methodology

1. Samples were produced by high pressure vacuum die casting and permanent mold casting;

2. TTT and TTP curves of samples were constructed by using interrupted quenching techniques;

3. Quench factor analysis (QFA) was used to predict the mechanical properties of the castings with various cooling rates;

4. Differential scanning calorimetry (DSC) tests and Avrami kinetics were performed in aid of comparing the quench sensitivity;

5. Optical microscope was applied to observe the microstructure of the samples in as cast condition and solution heat treated condition; scanning electron microscope (SEM) equipped with energy-dispersive X-ray spectroscopy (EDS) was used to give an element analysis; transmission electron microscopy (TEM) was utilised in the isothermal heat treated samples to study precipitates.

6. Electron backscatter diffraction (EBSD) were used to study the grain size and grain boundary;

Chapter 2 Review of literature

2.1 Al-Si alloy

With the development of automotive, electronics and aerospace industries, the demanding of light and high mechanical properties metal is increasing. As one kind of light metal alloys, the Al–Si alloys has an excellent combination of casting characteristics and mechanical properties[19].

Al-Si alloy contain high silicon content, which results of excellent castability and good corrosion resistance[20]. As shown in figure 2.1[21], the Al-Si binary system forms a simple eutectic at 577°C with 12.6% Si. It can also be seen that aluminum can dissolve a maximum of 1.62% Si into solid solution. Depending on the amount of silicon, the Al-Si casting alloys are divided into three groups[22] : hypoeutectic alloys with Si contents between 5% and 10%, eutectic alloys with 11%-13% Si, and hypereutectic alloys, commonly with a Si content between 14% and 20%. Generally, hypoeutectic and near eutectic Al-Si alloys are used when good castability and corrosion resistance are required, moreover, small additions of Mg and Cu are added in order to enhance their response to heat treatment. The increase in properties from heat treatment, results in an extensive use of these alloys in a variety of applications in the automotive, aerospace and military industry. However, the presence of large, brittle, acicular flakes and plates of eutectic silicon leads to a substantial reduction of strength and elongation of the castings[6, 7]. Modification of the eutectic silicon by small additions of Na or Sr results in a noticeable improvement in strength, and a significant increase in elongation[23-24].

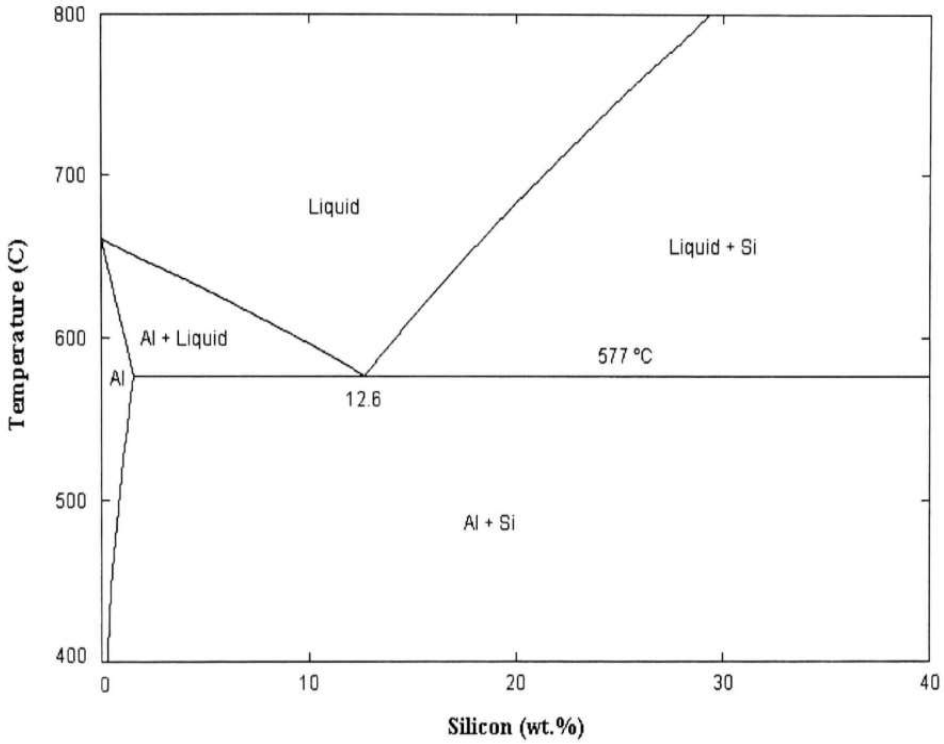

Figure 2.1: Equilibrium binary Al-Si phase diagram[21].

Aural^{TM} alloys as one of the Al-Si alloy is a family of high performance alloys specifically designed for demanding automotive safety and structural components, due to its superior light weight and high mechanical performance. Aural^{TM} alloys have a superior chemistry content that offers a good balance of strength and ductility, while also exhibiting excellent corrosion resistance. Due to their very good fluidity, these alloys are well suited to the casting of thin and large structural components[1].

Figure 2.2 is the binary phase diagram of Aural^{TM} alloys (Al-0.50wt%Mn-0.5 wt%Mg-0.18 wt%Fe-10 wt%Si) obtained by Thermo-calc software. It illustrates the Aural^{TM} 3 alloys phase diagram with the weight percentage of Si ranges from 0-12%. As we can see, with the increase of Si, the solvus temperature of Mg_2Si increases, and reaches the peak temperature (525°C) at 10

wt% of Si. Figure 2.3 is the binary phase diagram of Aural^{TM} series alloys (Al-0.50wt%Mn-0.2 wt%Mg-0.18 wt%Fe-7 wt%Si) with weight percentage of Si ranges from 0-7%. With 7 wt% of Si (Aural^{TM}-5), the solvus temperature of Mg_2Si is 475 ^{o}C. With the increase of element concentration, the solvus temperature also increases.

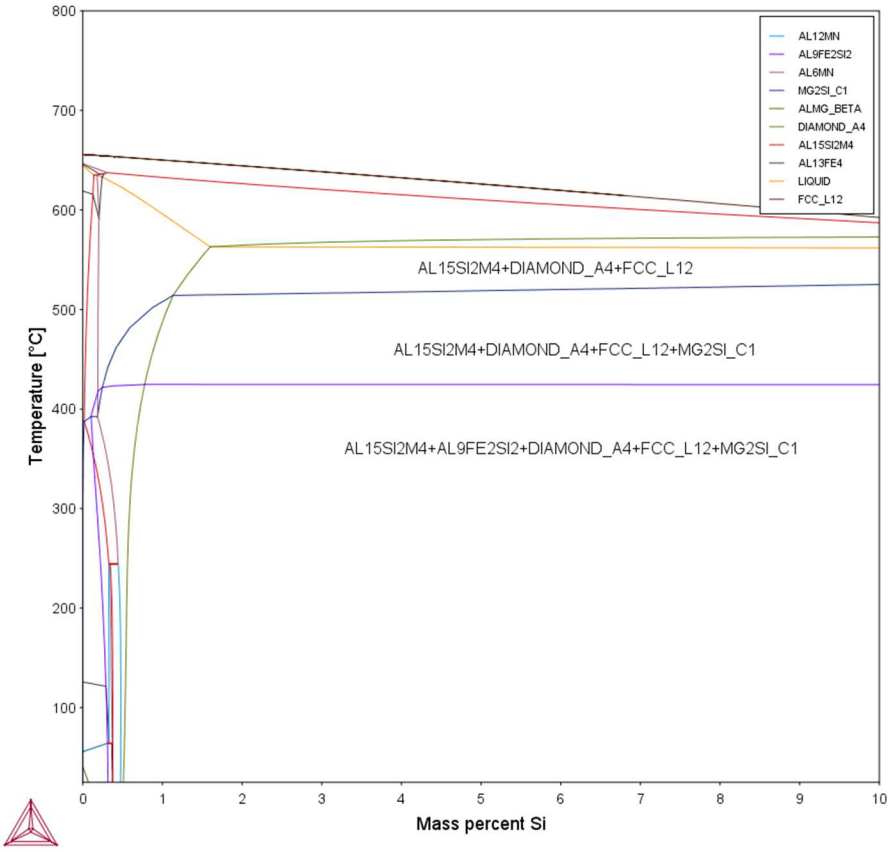

Figure 2.2:Pseudo binary phase diagram for Aural^{TM} alloys (Al-0.50wt%Mn-0.5 wt%Mg-0.17 wt%Fe-10 wt%Si).

.

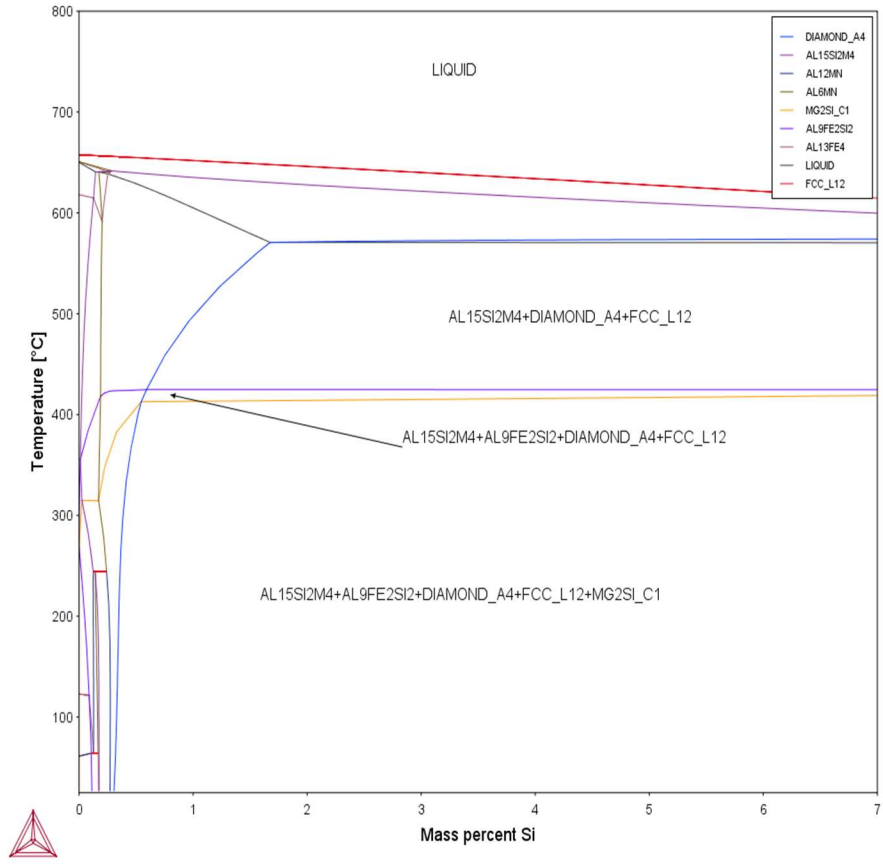

Figure 2.3: Pseudo binary phase diagram for Aural™ alloys (Al-0.50wt%Mn-0.2 wt%Mg-0.17 wt%Fe-7 wt%Si).

Table 2.1: the chemical composition of Aural™ alloys[25].

Variants	Aluminum	Silicon	Iron	Copper	Manganese	Magnesium	Zinc	Titanium	Strontium
Aural-2™	Remaining	10.3	0.16	<0.01	0.52	0.31	<0.01	0.05	-
Aural-3™	Remaining	10.1	0.18	0.01	0.49	0.55	<0.01	0.06	0.012
Aural-5™	Remaining	7.4	0.17	<0.01	0.49	0.20	<0.01	0.08	0.018

As shown in the table 2.1, the differences between Aural™-2 and Aural™-3 alloys are the addition of Mg and Sr. In Aural™-2 alloy, it has 0.31 wt% of Mg, which is much less than Aural™-3 alloy (0.55 wt% Mg). Since Magnesium Silicide (Mg_2Si), is the main strengthening phase for Aural™ alloys, the increased addition of Mg will contribute to higher mechanical property.

Meanwhile, the addition of Sr in Aural^{TM}-3 alloy will modify the morphology of the Si particle from needle shape into fibrous form, which increases the ductility.

The difference between Aural^{TM}-3 and Aural^{TM}-5 alloys are the addition of Si and Mg. In Aural^{TM}-3 alloy, it has 10 wt% Si addition compares to 7 wt% in Aural^{TM}-5 alloy. Moreover, Aural^{TM}-3 has twice as much Mg as in Aural^{TM}-5 alloy. The increased addition of both Si and Mg in Aural^{TM}-3 alloy will lead to higher mechanical property than Aural^{TM}-5 alloy.

2.2 Quench sensitivity

The tendency for an alloy to form non-hardnable precipitates during quenching is referring to as quench sensitivity[26] .Quenching is a significant step, because insufficient quenching often leads to a decrease in performance after ageing. When the quenching rate is relatively small, the coarse particles precipitate heterogeneously from the supersaturated solid solution and grow fast, leading to decrease in strength. However, excessive rapid cooling rate will increase the tendency for thick pieces to develop the severe residual stress and lead to distort[14] . Different alloys have different sensitivity to quenching rate, for a particular material, an appropriate quenching rate is necessary in order to maximize the mechanical properties and minimize the residual stress of the alloy.

The most straightforward approach for calculating quench sensitivity for a certain alloy after a continuous cooling process would simply be to introduce time-temperature-precipitation (TTP) and time-temperature-transformation (TTT) diagrams. Time-temperature-precipitation (TTP) diagrams deliver

important material data, such as quench sensitivity temperature and time ranges for precipitation during the quenching step of the solution heat treatment process. After mathematical calculations, isothermal TTP diagrams can be used to investigate continuous cooling processes. Ma et al.[27] investigated the quench sensitivity of Al-7 pct Si- 0.4 pct Mg (A356) solution heat treatment samples. They used quench factor analysis and constructed TTP curves, which has nose temperature at 425ºC, as indicated in the figure 2.4[27]. There are several factors that would affect quench sensitivity. Zhang and Zheng[19] investigated the quench sensitivity of Al-Si-Mg alloy, they found that the heat treatment process would affect quench sensitivity, as to the fact that the underaged condition was less quench sensitive than the peak-aged condition. Chaudhury and Apelian[28] investigated the quench sensitivity of Al-7 pct Si-Mg alloys with Mg content from 0.35-0.56 pct. They found that the alloy with the highest Mg content are the most sensitive to cooling rate, which implied highest quench sensitivity.

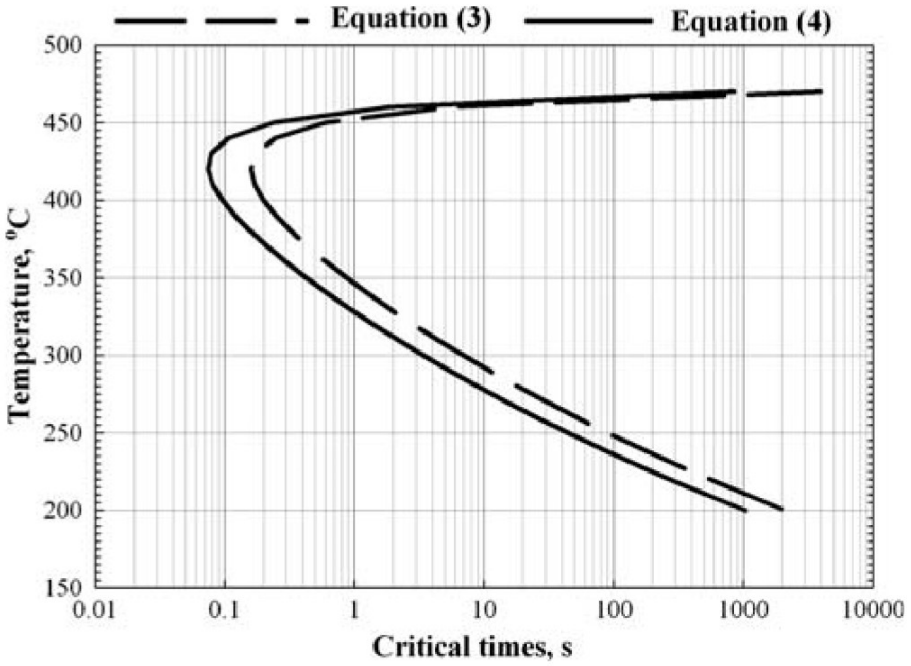

Figure 2.4: 99.5% TTP curves of A356 casting alloy, dash and solid indicate the TTP curves under different calculation[27].

2.2.1 Quench factor analysis

The Quench factor is defined as the severity of a quench and can be quantified to a single number using integrated cooling rate and TTP curves[29]. Quench factor has been generally used to predict properties under certain cooling rate.

When a precipitation hardenable alloy is cooled from above the solvus temperature, the change in free energy increases progressively as the difference between the present temperature and the solvus temperature increases. This change in free energy of the system with undercooling is the driving force for nucleation of a new phase. The nucleation rate I as a function of temperature T can be expressed as:

$$I = \beta \exp(-\Delta G_m / kT) \exp(-\Delta G^* / kT) \text{ …….(2.1)}^{15}$$

Where

ΔG^*=activation energy for nucleation

ΔG_m=activation energy for diffusion

k =Boltzmann's constant

β=parameter including density of potential nucleating sites

The nucleation kinetics of equilibrium precipitates, transition precipitates, and Guinier-Preston (GP) zones all show a C-shaped TTP behaviour. Nucleation rates are low at high temperatures (small undercooling) because the driving force for nucleation is small (low ΔG*). Precipitation rates are low at low temperatures (large undercooling) because diffusion kinetics are low (low ΔG_m)[15].

All terms in this equation are essentially independent of temperature, except for ΔG*; the main factor controlling ΔG* is the driving force for precipitation, ΔG_m. For a particular alloy, ΔG_m is proportional to the degree of undercooling. It can be expressed as a function of temperature:

$$\Delta G^* = K_s T_s^2 / (T_s - T)^2 \text{……..…..….(2.2)}^{15}$$

Where K_s is another constant. This expression was substituted in the reciprocal form of equation (2.1)[15] to give

$$C_t(T) = -k_1 k_2 exp\left[\frac{k_3 k_4^2}{12T(k_4 - T)^2}\right] exp\left(\frac{k_5}{RT}\right) \text{……..…..….(2.3)}^{15}$$

Where

$C_t(T)$ = the critical time for a certain amount of solute to precipitate

k_1 = the natural logarithm of the fraction unprecipitated during isothermal holding tests;

k_2 = the constant associated with the reciprocal of the number of nucleation sites;

k_3 = the constant corresponding to the nucleus energy;

k_4 = the constant related to the solvus temperature;

k_5 = the constant related to the activation energy for diffusion;

R = the mole gas constant;

T = the thermodynamic temperature;

This is also the equation that will be used to calculate TTP curves.

2.3 Effect of casting processes

Previous studies show that there are some influencing factors that would affect mechanical properties. It is widely agreed that the mechanical properties are affected by the microstructure of the material. Casting process, besides chemical compositions and heat treatment process is one of key variables controlled the microstructures as well as mechanical properties.

2.3.1 Casting processes

2.3.1.1 Permanent mold casting (PM)

Permanent mold casting is a metal casting process that employs reusable molds ("permanent molds"), usually made from metal, where molten metal is poured into a mold that is made in two halves. In permanent mold casting, the metal is poured either directly by gravity or by pouring the metal into a cup attached to the mold and tilting it from a horizontal to a vertical position, as

indicated in the figure 2.5[30]. The metal mold aids in quicker solidification of the casting material, which results in highly desirable fine-grained structures that have high strength and soundness[31]. Permanent mold requires high production volume to reduce its tool cost. However, the thermal fatigue and erosion usually limit the life of the molds. Thus, permanent mold considered as medium to high cost per part[32].

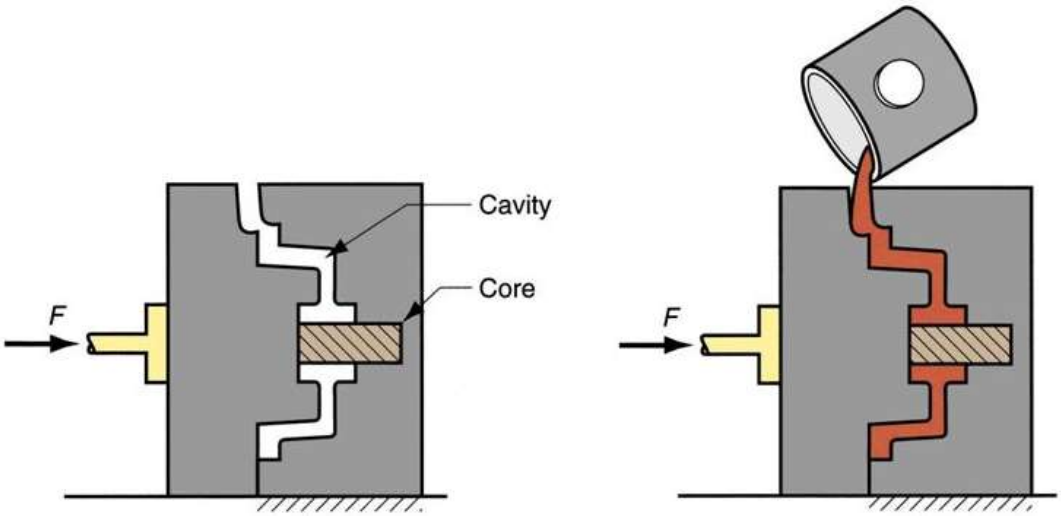

Figure 2.5: (a) Permanent mold casting process (a) before casting (b) during casting[30].

2.3.1.2 High pressure die casting (HPDC)

High pressure die casting (HPVD) production is economic and yields quicker results when compared to permanent mold casting. High pressure die casting can produce geometrically complex metal parts and is ideal for a large quantity of small- to medium-sized castings with low cost. It is a near-net shape manufacturing process in which molten metal is injected into a metal mould at high speeds and allowed to solidify under high pressures. It provides excellent

dimensional accuracy and the smooth surfaces[33].A schematic view of high pressure die casting is given in Figure 2.6[30].

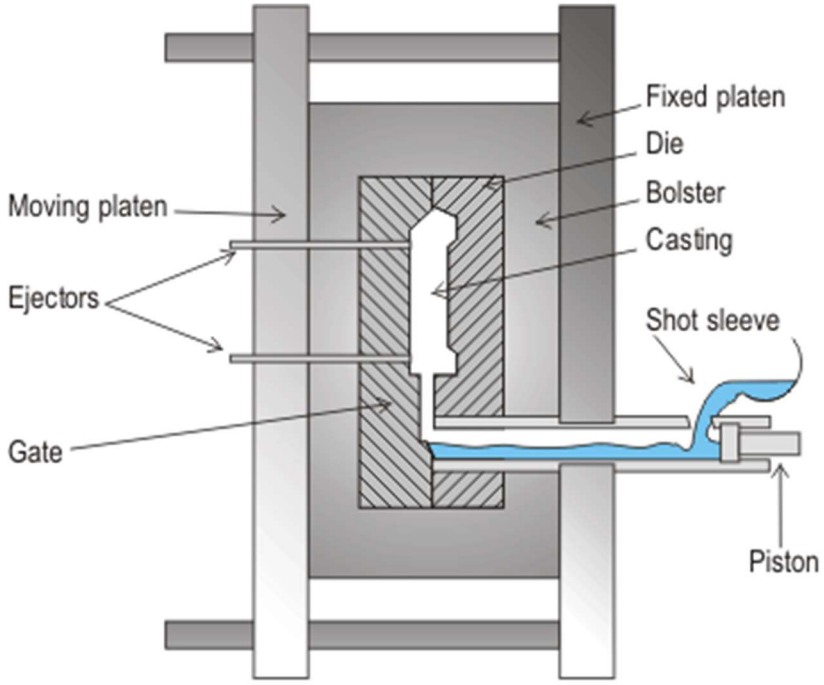

Figure 2.6 : Schematic view of a high pressure die casting machine[30].

However, the turbulence of the liquid alloy and the complex shape of the casting mold in die casting often result in porosity, since air and other gases are often trapped in the metal[2]. Porosity also affects the mechanical properties of the product as it can concentrate the stress and speed fracture[34]. The formed pores, especially the ones located adjacent to the casting surface, are likely to expand size during heat treatment, thus lead to blisters at the casting surface[35]. In consequence of that, the die castings are normally non-heat treatable, that limits the application of the aluminium die castings. However, with the joint of vacuum system, almost all the air is positively evacuated from the mold, which largely reduces porosity[36]. In contrast to that, permanent mold castings typically contain

lower levels of entrapped gas, resulting in superior pressure tightness and soundness.

2.3.1.3 High pressure vacuum die casting

In high pressure vacuum die casting process, a vacuum valve is added into a die to evacuate the entrapped air in the cavity, thus creates a vacuum casting environment. As a result, the number density of the porosity is largely reduced. The potential applications for the high pressure vacuum die casting process are for the production of high integrity die casting components that require pressure tightness and good mechanical properties via heat treatment. Figure 2.7[36] illustrates the principle of the high pressure vacuum die casting process. After the metal was ladled into the injection chamber, the plunger moved past the pouring hole and sealed off the die cavity (Figure 2.7(a)). The vacuum valve was then activated and a lower than atmospheric pressure was created in the die cavity. The cavity was evacuated continuously from the beginning of die filling to the end (Figure 2.7 (b)).

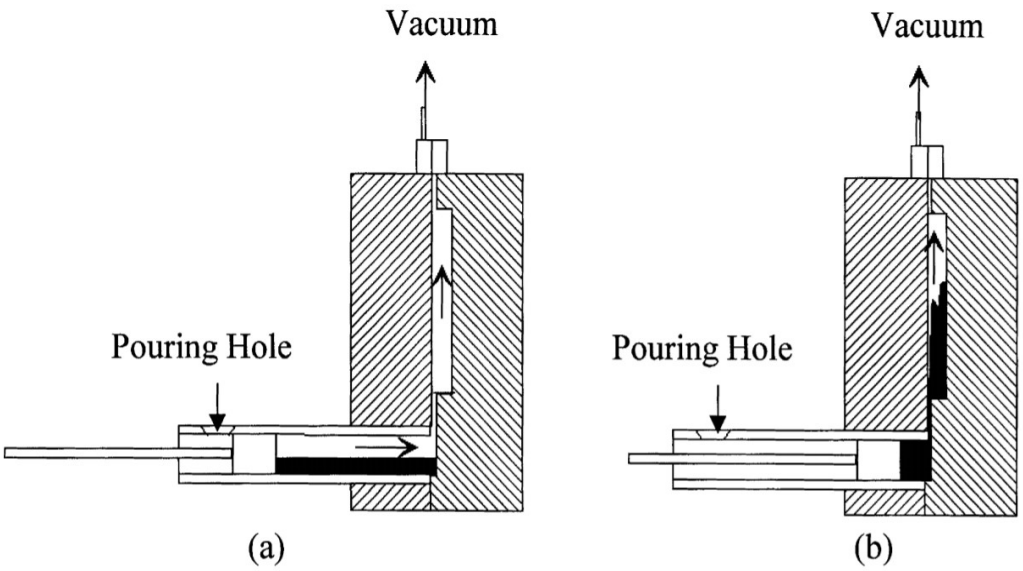

Figure 2.7:The principle of the high pressure vacuum die casting process[36].

Figure 2.8[36] illustrates the micrographs of the cross-section of the Al-8%Si alloy under different casting processes. It shows that the high pressure die casting has higher number density of gas porosity than high pressure vacuum die casting.

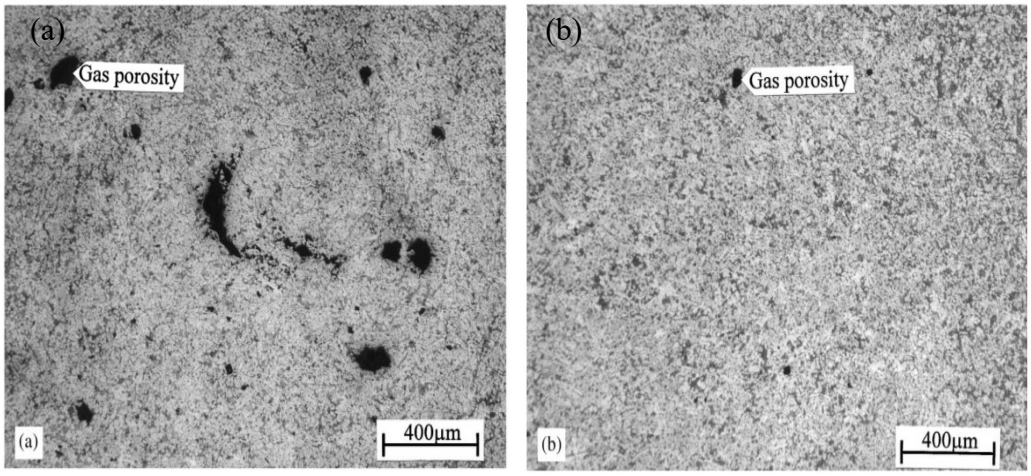

Figure 2.8: micrographes of the cross-section of the Al-8%Si alloy, showing the porosity distribution in: (a) high pressure die casting (b) high pressure vaccum die casting[36].

2.3.2 Effect of casting process on quench sensitivity

Different casting processes have different casting process parameters, for example injection speed, casting pressure and cooling rate, thus produce different microstructures. There is a wide agreement that the mechanical properties are affected by the microstructure of the material[37]. Okayasu et al.[17] studied the mechanical properties of an Al–Si–Cu alloy (ADC12) produced by various casting processes. Figure 2.9[17] illustrated the microstructure of the castings under high pressure die casting (HPDC) and permanent mold casting (PM) in as cast condition. They found that the microstructure of PM samples was formed mainly with coarse α-Al phase and needle shaped Si and Fe based eutectic structures. In contrast, a fine round α-Al phase and fine eutectic structures were observed for the HPDC. Due to fine round α-Al phase and fine eutectic structures, ultimate tensile stress and strain to failure for HPDC samples are higher than those for the PM samples. In addition, HPDC samples has higher hardness than PM in as cast condition. Those differences were caused by the solidification rate. In HPDC, high inject rate and high pressure produced fine microstructure, following by high mechanical properties.

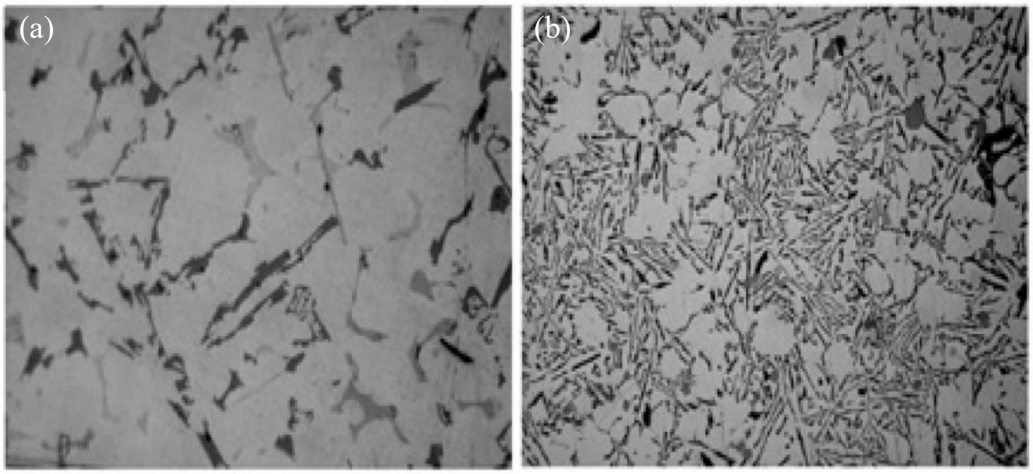

Figure 2.9: Microstructures of (a) Permanent mold casting, (b)high pressure die casting[17].

When the difference between the microstructures is excessively large, the impact of microstructure on the precipitation behavior cannot be ignored. Precipitation in solids is almost always heterogeneous[38]. Suitable nucleation sites are non-equilibrium defects such as excess vacancies, dislocation, grain boundary, stacking faults, inclusions, and free surfaces, all of which increase the free energy of the material[38]. If the creation of a nucleus results in the destruction of a defect, some free energy will be released thereby reducing (or even removing) the activation energy barrier[38]. The other planar defects such as inclusion/matrix interfaces, stacking faults can behave in a similar way to grain boundaries in reducing activation energy barrier[38]. However, the stacking flaults are much less potent sites due to their lower energy in comparison to grain boundary[38]. If the casting process results in large discrepancy in grain size as well as the amount of grain boundary between the two alloys, that difference would affect the precipitation behaviour during quenching, leading to a difference in quench sensitivity.

2.4 Effect of chemical composition

2.4.1 Effect of Magnesium on quench sensitivity

Magnesium (Mg) is one of the important elements found in Aural™ series aluminum alloys. Mg can associate with Si and form the compound Mg_2Si phase in the dendritic primary. In general, the Mg_2Si precipitation sequence expected upon aging remains: GP zone--β" --β' --β. Stoichiometry dictates that there are 2 Mg atoms for every Si atom in this compound. The equilibrium phase Mg_2Si or β- Mg_2Si is usually Mg enriched. Metastable states such as β'- Mg_2Si and β"- Mg_2Si are typically silicon enriched. Having an excess of Si will meet the requirement of free energy thus predominance the metastable states. Mg enrichment will promote the formation of the equilibrium phase[11].

After manufacturing, the alloys can sometimes be age hardened directly (T5 temper) or solutionized and then age hardened (T6 temper). The faster the alloy is quenched after the manufacturing operation for a T5 temper or after the solution treatment for a T6 temper, the less likely the non-hardening Mg_2Si phase will precipitate during quenching. Ideal hardening phases are β"- Mg_2Si. The optimized aging treatment after solution heat treatment should be designed to precipitate β"- Mg_2Si [39]. However, the non-hardening phase such as β'- Mg_2Si or β- Mg_2Si would precipitate during slow quenching, consuming large amount of Mg and Si solutes. The reduction of solute after quenching leaded to the decrease of strengthening phase in artificial aging, which ultimately decreased the hardness. Chaudhury and Apelian[28] investigated the quench sensitivity of Al-7 pct Si-Mg alloys with Mg content from 0.35-0.56 pct. They found that alloy

with the highest Mg content are the most sensitive to cooling rate, which implied highest quench sensitivity. Tiryakioglu and Shuey[18] investigated the quench sensitivity of D357 (Al-7Si-0.6Mg) casting alloys by constructing TTP curves and compared it to 6061 (Al-0.7Si-0.9Mg) wrought alloy, as shown in the figure 2.10[18]. They found that 6061 has higher quench sensitivity due to the fact that it has higher nose temperature and shorter critical time. The difference is caused by the chemical composition. As both alloys contain excessive Si levels, the low Si content of 6061 wrought alloy had a little impact on quench sensitivity. However, the 0.3 pct extra Mg addition greatly increased the supersaturation solubility which leaded to an increase of driving force of precipitation during quenching and increased the quench sensitivity.

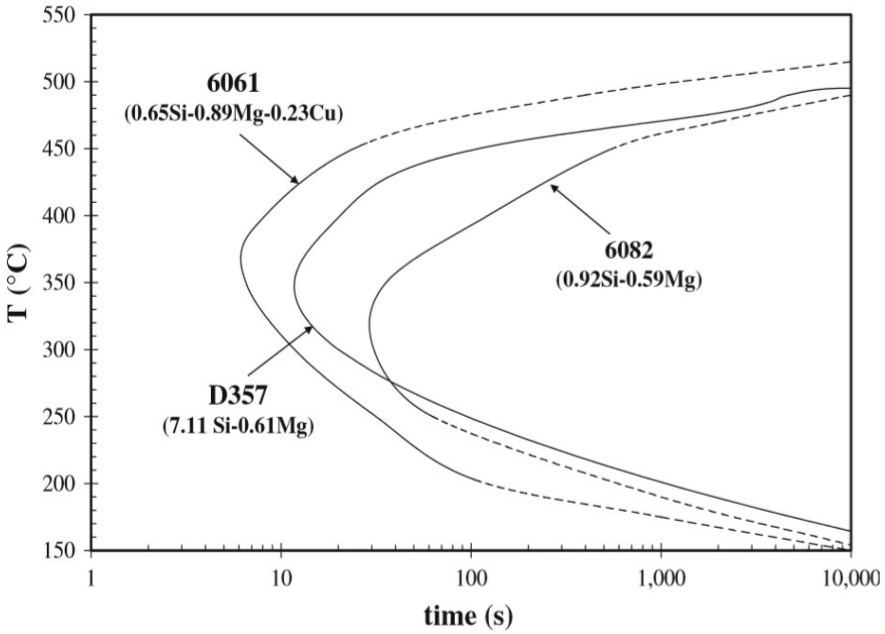

Figure 2.10: 95 pct iso-yield strength contours in three Al- Mg_2Si alloys[18].

2.4.2 Effect of Silicon on quench sensitivity

Silicon (Si) additions can improve the mechanical properties, such as modulus, strength, hardness and wear resistance of Al alloys and reduce the density and coefficient of thermal expansion[40]; however, the shape of the Si phase is usually acicular, thus results in poor tensile properties[6]. Modification can change the morphology of the Si particles from needle shape into fibrous form[41].

Due to its high fluidity and low shrinkage, Si has excellent castability. Its low solubility and high hardness in Aluminum improve the abrasion resistance. Si reduces thermal expansion coefficient of Al-Si alloys[8]. Machinability is poor with addition of silicon in Aluminum[42].

G.T. Abdel-Jaber et al.[40] investigated the mechanical behaviour of Al-Si alloy against silicon content. It was found that with the increase of Si content from 3% to 12% the hardness increases. Zhang and Zheng[19] studied the quench sensitivity of Al-7 pct Si- 0.4 pct Mg (A356) permanent mold (PM) casting alloy and compared it to 6063 wrought (Al-0.6 pct Mg-0.4 pct Si) alloy. They reported that excessive Si content would act as nucleation sites and increase quench sensitivity. Robinson[43] speculated that the increasing hardness drop during isothermal test holding at 450ºC with the prolonging of the holding time is not only because of the growth of β" or β' to larger size β which has much less strengthening effect than the former, but also because of loss of Si in solution by its diffusion to eutectic Si particles. The study has been also proved by Tiryakioglu and Shuey[18]. They investigated the quench sensitivity of D357 (Al-

7pct Si-0.6pct Mg) casting alloy. They reported that the quench sensitivity of D357 alloy is due to (a) the loss of Si to eutectic particles, (b) precipitation of β on eutectic Si particles, and (c) precipitation of β in the aluminum matrix. They also compared the D357 casting alloy to 6082 wrought alloy. The high quench sensitivity of D357 is due to the presence of Si particles. Zhong found that an excess of Mg slows down the natural aging process[44].

2.4.3 Effect of Manganese on quench sensitivity

There are two ways to modify the morphology of β-Al5FeSi: postsolutionizing cooling rate and chemical modification[45]. Alloying elements such as Mn has been used to replace the acicular β-phase with α-Al(Mn,Fe)Si which has granular or skeleton (or Chinese script) morphology, shown in figure 2.11[41]. Mn can also control the recrystallization via the formation of dispersoids[46].

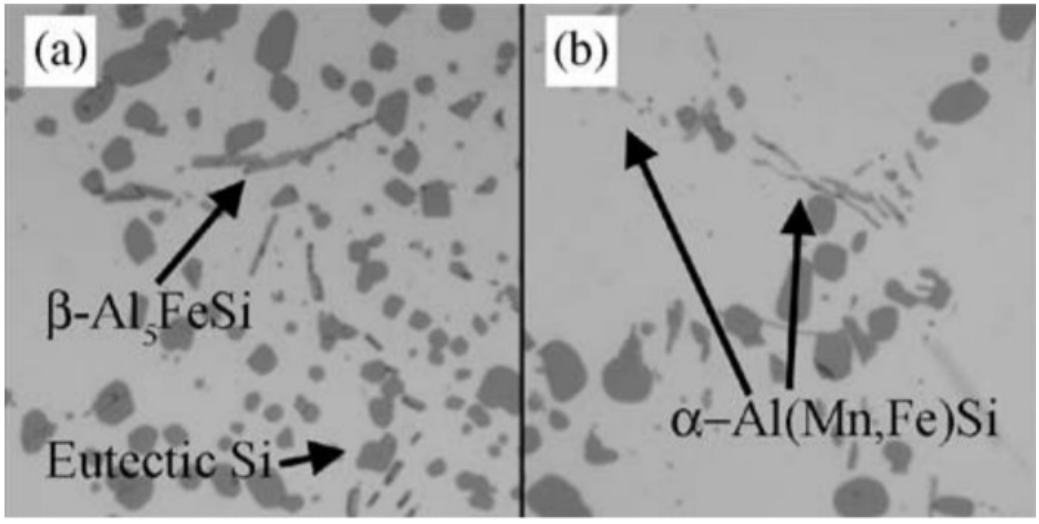

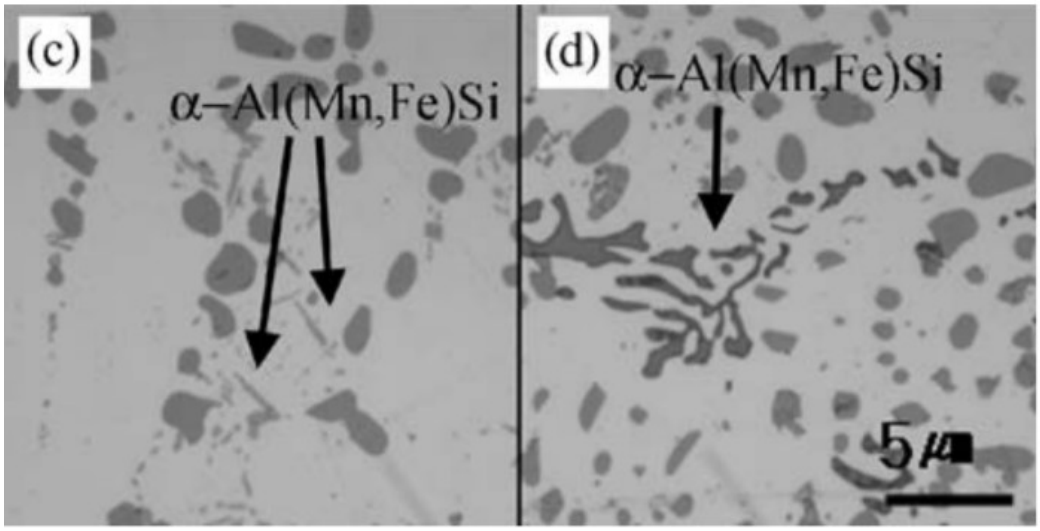

Figure 2.11: Morphology of a-Al(Mn,Fe)Si particles depending on the Mn content. Acicular b-AlFeSi particles in: (a) A356-0.20Fe alloy; (b) A356-0.20Fe- 0.07Mn alloy; (c) A356-0.20Fe-0.13Mn alloy; and (d) A356-0.20Fe-0.20Mn alloy[41].

The dispersoids formed during solution heat treatment can achieve strengthening effect of solute solution. Rometsch et al.[47] reported that the density of Mn containing dispersoids in cast and homogenised 6082, which are nucleation sites for non-hardening precipitates, such as β'- Mg_2Si and β''- Mg_2Si, and result in an increase of quench sensitivity. Robson[48] investigated microstructural evolution during quenching from homogenization. They found a large amount of Mg(Zn_2, AlCu) M-phase particles precipitated on Al_3Zr dispersoids, as shown in figure 2.11[48]. This study confirmed that the dispersoids would act as nucleation sites for precipitates during quenching. Mn dispersoids would affect quench sensitivity by influencing the precipitation behavior during quenching.

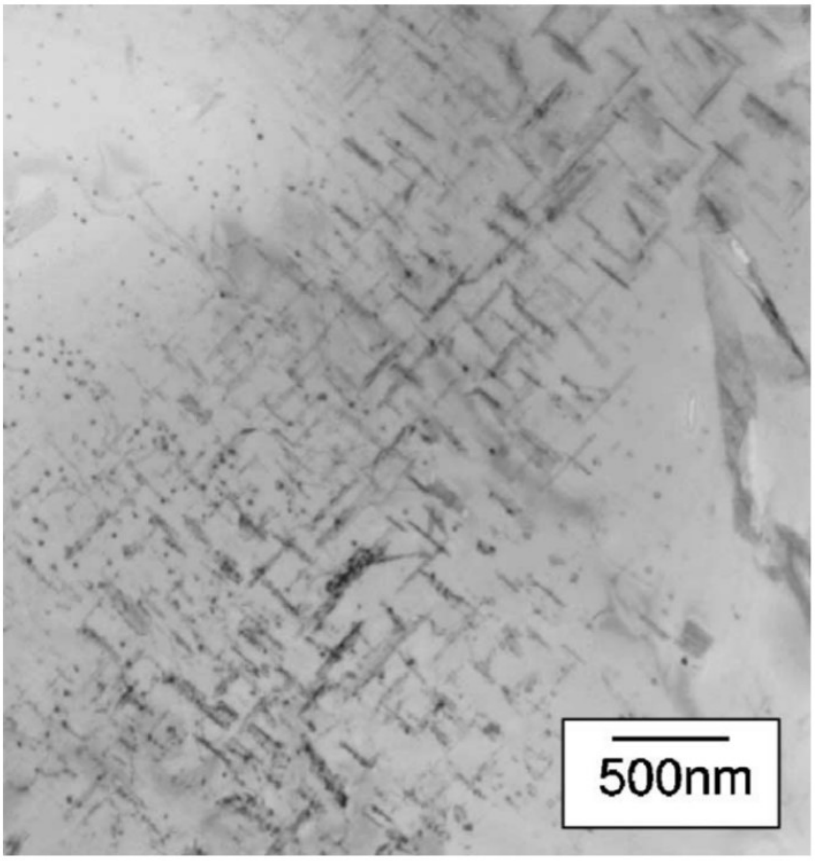

Figure 2.12: TEM micrograph of 7050 wrought alloy slow cooled to room temperature showing a band of Mg(Zn_2,AlCu) M-phase particles precipitated on Al_3Zr dispersoids[48].

Chapter 3 Experimental procedures

3.1 Sample preparation

The materials selected in the present study are the cast aluminum alloy Aural^{TM}-3 and Aural^{TM}-5. In this work, Aural^{TM}-3 alloy was produced by two different casting processes: (i) permanent mold casting (PM), (ii) high pressure vacuum die-casting (HPVD). Aural^{TM}-5 alloy was produced by HPVD. For the permanent mold casting, the AlSi10Mg alloy was prepared with commercially pure Al (99.7%), pure Mg (99.9%), Al-25%Mn, Al-25%Fe, and Al-50%Si master alloys. For each batch, approximately 3 kg of materials were melted in an electrical resistance furnace. The melt was kept at 720-750 ºC for 30 min and degassed for 15 min, and then poured into a permanent copper mold preheated at 250 ºC. The dimension of the cast plates is 100 mm x 80 mm with a thickness of 4 mm. The HPVD castings were produced by a cold chamber vacuum die casting machine, provided by Rio Tinto Aluminum. The dimension of the cast plates is 220 mm x 65 mm with a thickness of 2.5 mm. The chemical compositions of samples analyzed by an optical emission spectrometer are listed in Table 3.1. Some cast specimens were also subjected to T6 heat treatment with the solution treatment at 500 °C for 1 h followed by the aging at 170 °C for 2.5 h, shown in figure 3.1.

Table 3.1: Chemical compositions of experimental alloys (wt.%)

Alloys	Castings	Si	Mn	Mg	Ti	Sr	Fe	Al
Aural™ 3	PM	10.10	0.50	0.59	0.08	0.012	0.20	bal.
Aural™ 3	HPVD	10.10	0.50	0.55	0.08	0.011	0.18	bal.
Aural™ 5	HPVD	7.40	0.49	0.20	0.08	0.018	0.17	bal.

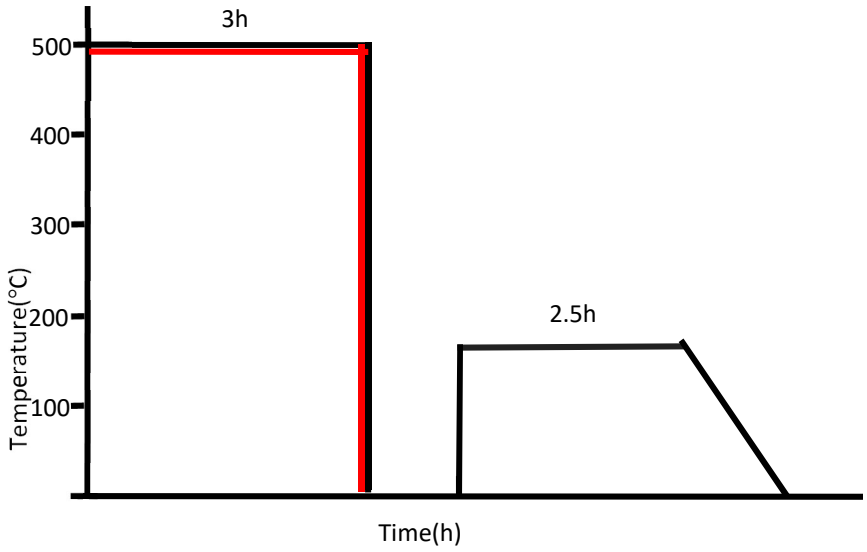

Figure 3.1 : Red line: solution treatment (T4 : 500°C for 3h), Black lines: solution+aging treatment(T6: 500°C for 3h and 170°C for 2.5h).

3.2 Microstructure Characterization

3.2.1 Optical Microscopy (OM)

Samples were cut into rectangular shape (high pressure vacuum die casting 20mm× 20mm× 2.5mm; permanent mold casting 20mm× 20mm× 4mm), and vertical mounted with graphite powder. Conventional metallographic polishing was applied for the sample preparation. Samples were first polished with emery papers with increasing grit size (120, 220, 320, 600) and fine polished with 6 μm and 1 μm diamond abrasive. The final step 0.05 μm polishing was done with a

colloidal silica suspension. The microstructure variables in five zones along the sample cross section were analyzed with image analysis. In each zone, eight optical images (500x) were quantitatively analyzed.

An optical microscope (Nikon Eclipse ME600 machine) with an image analyzer (CLEMEX software PE4-0), as shown in figure 3.2, was used for observation and quantitative characterization of the microstructural variables, such as the equivalent diameter, aspect ratio, volume fraction, distribution of various phases.

Figure 3.2: Clemex image analysis system with Nikon Eclipse ME600 optical microscope.

3.2.2 Scanning Electron Microscopy (SEM)

A scanning electron microscope (SEM, JSM-6840LV) equipped with an energy dispersive spectrometer (EDS), as indicated in figure 3.3, was employed to observe and characterize different types of phases.

Figure 3.3: JEOL JSM-6480LV SEM system

3.2.3 Electron Backscatter Diffraction (EBSD)

EBSD specimens were ground with grit abrasive paper with grit size from 120 to 600 and polished using 6 μm and 1 μm diamond paste. The samples were then polished with 0.05 μm non-crystallizing colloidal silica without water addition for 5 minutes. EBSD patterns were obtained through SEM.

3.2.4 Transmission electron microscopy (TEM)

TEM samples were cut from the cross section of the plate, and grinded to about 60μm thickness. Double-jet electro-chemical polishing were applied on the samples in a solution of 15% nitric acid and 85% methanol at -25 ºC and at a voltage of 20V. TEM observation was conducted by the JEM-2100 transmission electron microscopy, as shown in figure 3.4.

Figure 3.4: JEM-2100 transmission electron microscopy.

3.2.5 Electrical Conductivity testing

For conductivity testing, the standard test method for determining the resistivity of electrical conductor materials is ASTM B 193-87. Conductivity is calculated from the measured resistance and dimensions of the specimen. The accuracy and convenience with which resistance can be measured depends on the actual resistance of the specimen. The conductivity of aluminum alloys is

used to correlate to the extent of solutes retained in solid solution[49]. It is a function of the microstructural state of the matrix alloy[49]. It is inversely proportional to the volume of the precipitates and is proportional to the quantity of the precipitates. Temperature has a huge impact on the results[49], thus each test was calibrated by standard aluminum test sample— bringing standards to sample temperature. The electrical conductivities of the samples were obtained by Sigmascope SMP10 unit. Each side of samples was measured 2 times. The average electrical conductivity of 4 tests were obtained.

3.2.6 Differential scanning calorimetry (DSC) testing

Differential scanning calorimetry (DSC) analyses were performed using a DSC 8000, a computerized differential scanning calorimeter at a heating rate, 10°C/minute, from room temperature to 570 °C. The average data of three samples for each type of castings were reported. Four-millimeter diameter disc samples with mass about 30 mg were cut out from solution treated cast plates.

3.3 Mechanical Characterization

3.3.1 Tensile testing

The tensile tests were carried out at room temperature using an Instron universal testing machine according to the ASTM B557. Sub-size tensile test bars (100 mm in the overall length and 25 mm in the gage length) were used. Figure 3.5 showed the ASTM E8/E8M standard for a sub-size tensile specimen.

Tensile specimens were heat treated according to the T4, T6 thermal profiles in figure 3.6. The tensile properties, namely the ultimate tensile strength (UTS), yield strength (YS) at a 0.2% offset strain and fracture elongation (El), were reported as an average value of four test bars.

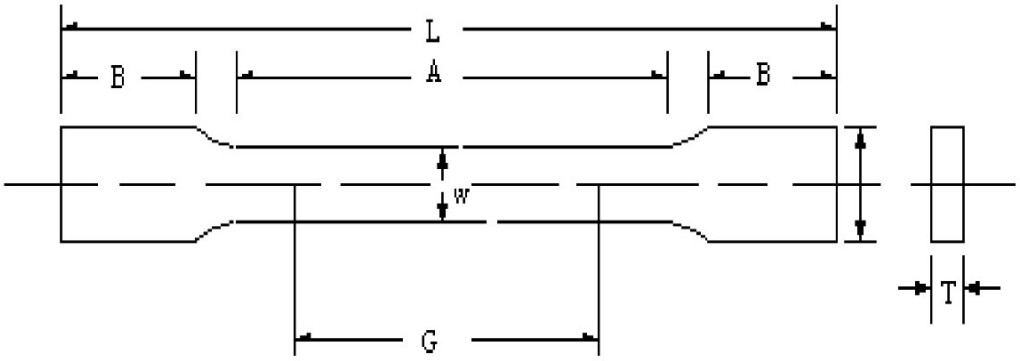

Figure 3.5: Schematic illustration of Tensile Test Specimen

G – Gage length: 25.0 ± 0.1 mm;

W – Width: 6 ± 0.1 mm;

T – Thickness: 3 ± 0.1mm;

R – Radius of fillet, min: 6 mm;

L – Overall length, min: 100mm;

A – Length of reduced section: 32 mm;

B – Length of grip section, min: 30 mm;

C – Width of grip section: 10 mm.

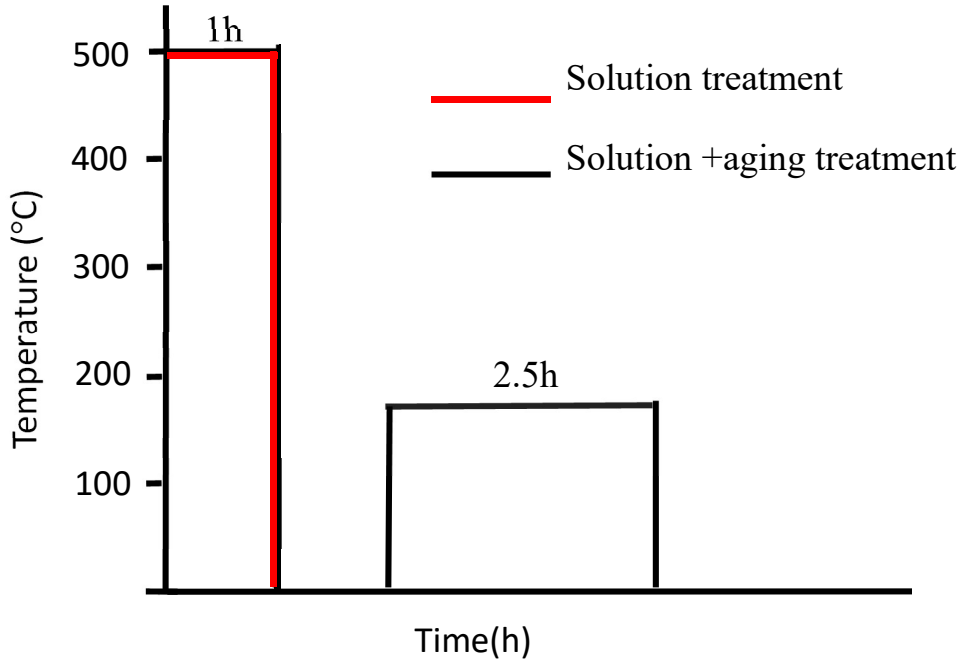

Figure 3.6: Red line: solution treatment (T4 : 500°C for 1h), Black line: solution+aging treatment(T6: 500°C for 1h and 170°C for 2.5h)

3.3.2 Micro-hardness testing

In order to measure Vickers hardness, a flat and polished surface is required. The standard metallurgical preparation procedure was used to prepare the sample. Samples were first polished with emery papers with increasing grit size (120, 220, 320, 600) and fine polished with 6 µm and 1 µm diamond abrasive. The final step 0.05 µm of polishing is done with a colloidal silica suspension. Vickers hardness measurements were performed using Nextgen NG-1000CCD hardness test machine with a load of 100 g and 15 s dwell period on the polished surface following the ASTM E92. The sample was then placed in the Nextgen machine. Lines were made along the 2 diagonals of the diamond indents; both diagonals

were entered the Vickers hardness formula shown in the following equation, and auto-calculated by Nextgen.

$$HV = \frac{2P\sin\left(\frac{136^{O}}{2}\right)}{d^2} = \frac{1.8544P}{d^2} \quad \text{……..(3.1)}$$

where P is the load in kgf and d is the length of the diagonal in micronsThe data, minimum 10 measurements, was then averaged over all the points taken on each specimen.

3.4 Quench factor analysis

3.4.3 Interrupted quench techniques for time-temperature-precipitate curves

In order to meet the requirement of isothermal tests. All the samples were cut into square plate with dimensions 20×20×2.5mm (HPVD) and 20×20×4mm (PM). Samples were solute-heat treated at 500℃ for 3h, and immediately transferred into a salt bath and held isothermally at temperatures ranging from 250-450ºC for set period. Subsequent quenching was done in water at room temperature. Then all the samples were artificial aged at 170ºC for 2.5h. Ultimately, the samples were prepared via the standard metallurgical sample preparation method for Vickers hardness measurements. Figure 3.7 showed a schematic of the different heat treatments used to conduct these tests.

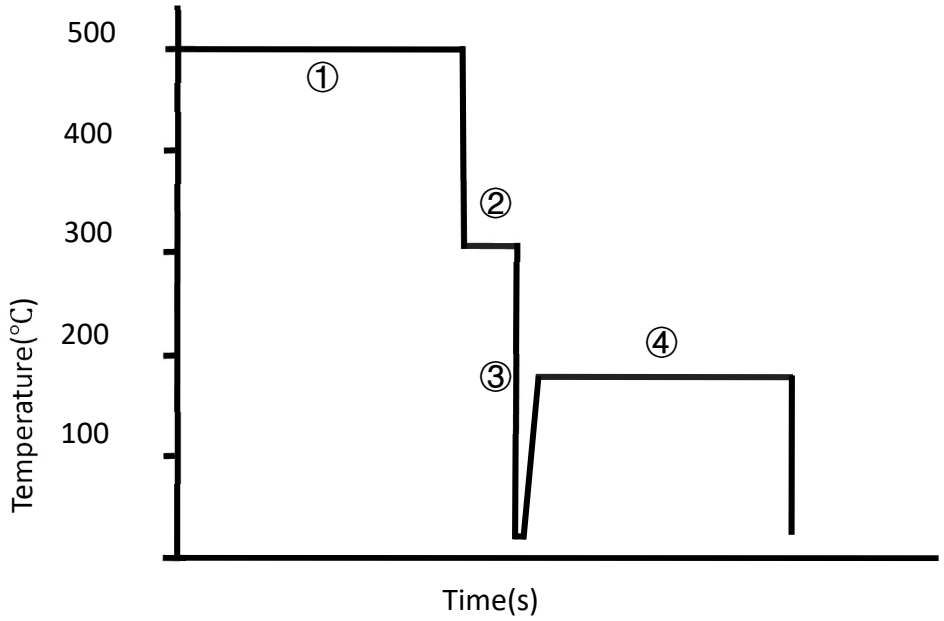

Figure 3.7: Schematic of heat treatments used in the procedure for time-temperature precipitates tests

1. Solution heat treatment under 500℃for 3h;
2. Soaking steps at different temperatures(250℃-450℃) and different time(10s-1800s);
3. Water quench to room temperature;
4. Aging at 170℃ for 2.5h.

3.4.4 Instrumentation and Cooling Curves

The cooling rates of each sample are important to calculate because there is a direct correlation between cooling rate and the mechanical properties after the T6 treatment. To do this for the HPVD and PM samples, the samples had to be instrumented with thermocouples. 1mm holes were drilled from the cross section of the sample and move through the sample in the axial direction. The holes were drilled 10mm deep. This was done to reflect the temperature at the middle of the sample to represent the sample temperature. K+ thermocouples were used to

collect the data. Samples were heated at 500ºC for 3h and immediately cooled in different media to obtain different cooling rates. The data collected from the thermocouples was done using Graphtec GL240 data logger. Due to the nature of these alloys the important transformations occur during the moderate temperature range of each alloy which will be obtained after constructing the time-temperature-precipitate curves. Based on this information the average cooling rate was calculated between this temperature range. The average cooling rate was calculated by averaging the first derivative between the temperatures of 450°C to 250°C. The data was then taken from these calculations and matched up with hardness values.

3.4.5 Continuous cooling tests

To evaluate the suitability of predicted and experimental results. Continuous cooling tests were conducted. Samples were sectioned from initial casting alloy and instrumented with Type K thermocouples in the center of the sample. After solution heat treatment at 500ºC for 3h, samples were quenched immediately (less than 3s) by various means (still or flowing air, fiberglass insulator, oil with different temperature) shown in fig. 10, and artificial aged at 170 ºC for 2.5h, followed by Vickers hardness tests. This allows us to assess the suitability of the experimental calculation.

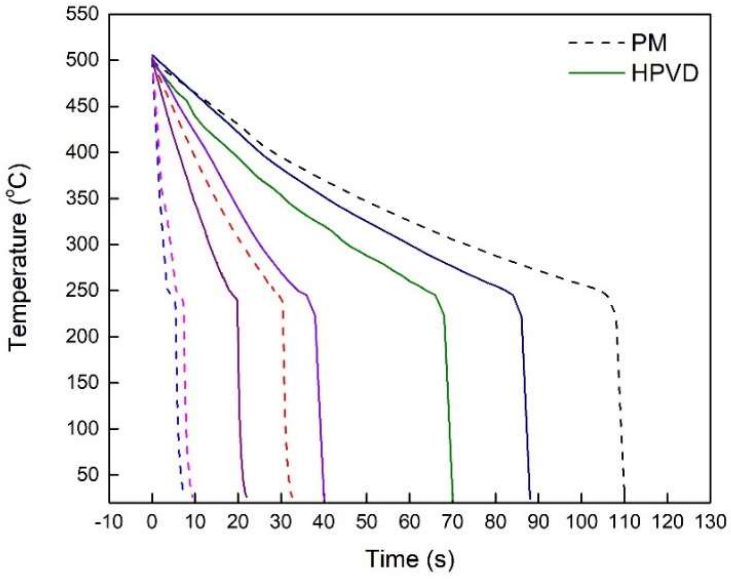

Figure 3.8: Cooling curves for HPVD (line) and PM (dash).

3.4.6 Interrupted quench techniques for time-temperature transformation curves

Similar to isothermal tests for time-temperature precipitate curves, the specimens for time-temperature transformation were solute-heat treated at 500℃ for 3h, and immediately transferred into a salt bath and held isothermally at temperatures ranging from 250-450ºC for set period of time. Subsequent quenching was done in water at room temperature, and artificial aging was done at 170ºC for 2.5h. Electrical conductivity tests were conducted after that. Figure 3.9 illustrated a schematic of the different heat treatments used to conduct these tests.

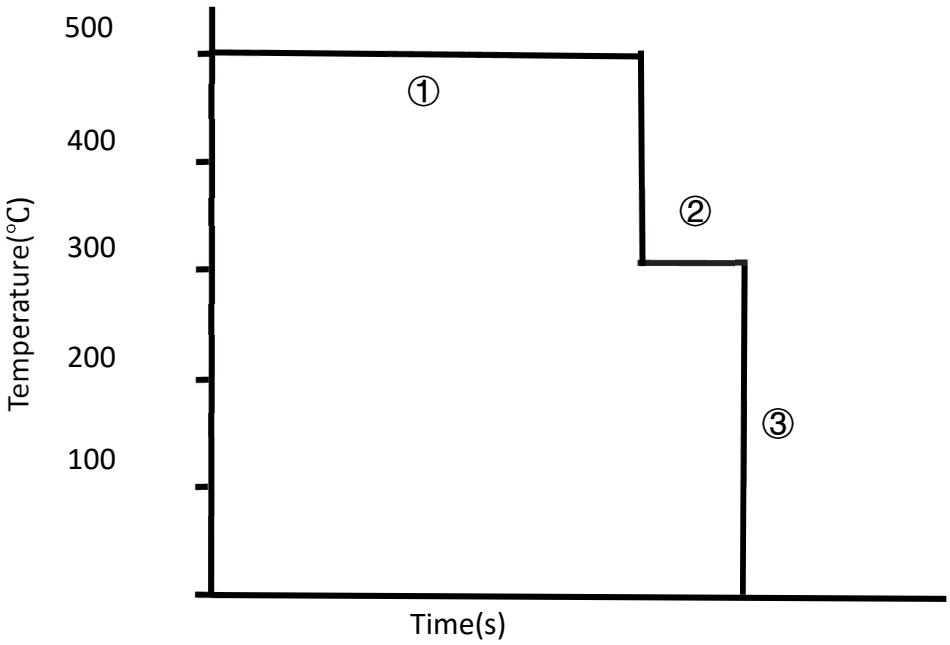

Figure 3.9: Schematic of heat treatments used in the procedure for time-temperature transformation tests

1. Solution heat treatment under 500℃for 3h;
2. Soaking steps at different temperatures(250℃-450℃) and different time(10s-1800s);
3. Water quench to room temperature.

Chapter 4 Results and discussion

4.1 Microstructures and mechanical properties of Aural™ 3 HPVD and PM

4.1.1 Microstructure of HPVD and PM samples

Figure 4.1 showed the optical and SEM images of the HPVD microstructure. Under optical microscopy, the rosette-like aluminum grains present with a light color, Al-Si eutectic is grey color and primary Mg_2Si particles show dark color (Figure 4.1(a) and (b)). The Fe-rich intermetallic phase can be better observed under SEM backscattered images (Figure 4.1(c) and (d)), which are the dot- and block-like particles with white color. The surface layer in HPVD castings has a unique feature and consists of 1) a skin sublayer, 2) a eutectic-rich sublayer and 3) an aluminum grain-rich sublayer, as indicated in Figure 4.1(a). The skin sublayer is directly adjacent to the sample surface with 60-100 μm in thickness, in which the size of aluminum grains and silicon particles is much smaller than that in the center position (Figure 4.1(b)). Next to the skin sublayer, it is a eutectic-rich sublayer, in which the fraction of Al-Si eutectic is much more than the other positions of the sample. Adjacent to the eutectic-rich sublayer, there is an aluminum grain-rich sublayer. After the surface layer (approximately 180-200 μm) towards the center, the microstructure becomes uniform as shown in Figure 4.1(b). In a particle suspension system, fluid flow affects the particle distribution[50]. In the HPVD die cavity filling process, the melt flow contains many aluminum grains, which are at first solidified in a shot chamber or on the die wall, and some of the aluminum grains would then dropped off from the wall

under the melt flow action. The skin sublayer forms on die cavity wall when the melt enters the cavity from a gate due to the high cooling rate on the wall. A shear force arises between the solidified skin sublayer on die cavity wall and the melt flow. Under the shear force, solute-rich liquid aluminum is concentrated on the interfaces (solidified skin sublayer/melt) to reduce the flow resistance, and the aluminum particles/grains are pushed to one side. Consequently, this results in the formation of a eutectic-rich sublayer and an aluminum grain-rich sublayer.

The quantitative image analysis results of the HPVD microstructure are shown in figure 4.2. The secondary dendrite arm spacing (SDAS) and aluminum grain size vary from the cast surface to the center (figure 4.2 (a)). The average value of SDAS in the skin sublayer (2.5 μm) is much smaller than that at the center (6 μm). The aluminum grains size varies along the cross section of the HPVD sample (figure 4.2 (a)) and increases from the cast surface toward the center. The equivalent diameter of the aluminum grains in the skin sublayer (4.2 μm) is approximately 60% of that in the center (7.2 μm). The similar phenomenon is observed on the eutectic Si and primary Mg_2Si particles as well as Fe-rich intermetallic particles, i.e. the size of those phases increases with increasing distance from the cast surface to the center (figure 4.2 (b), (c) and (d)).

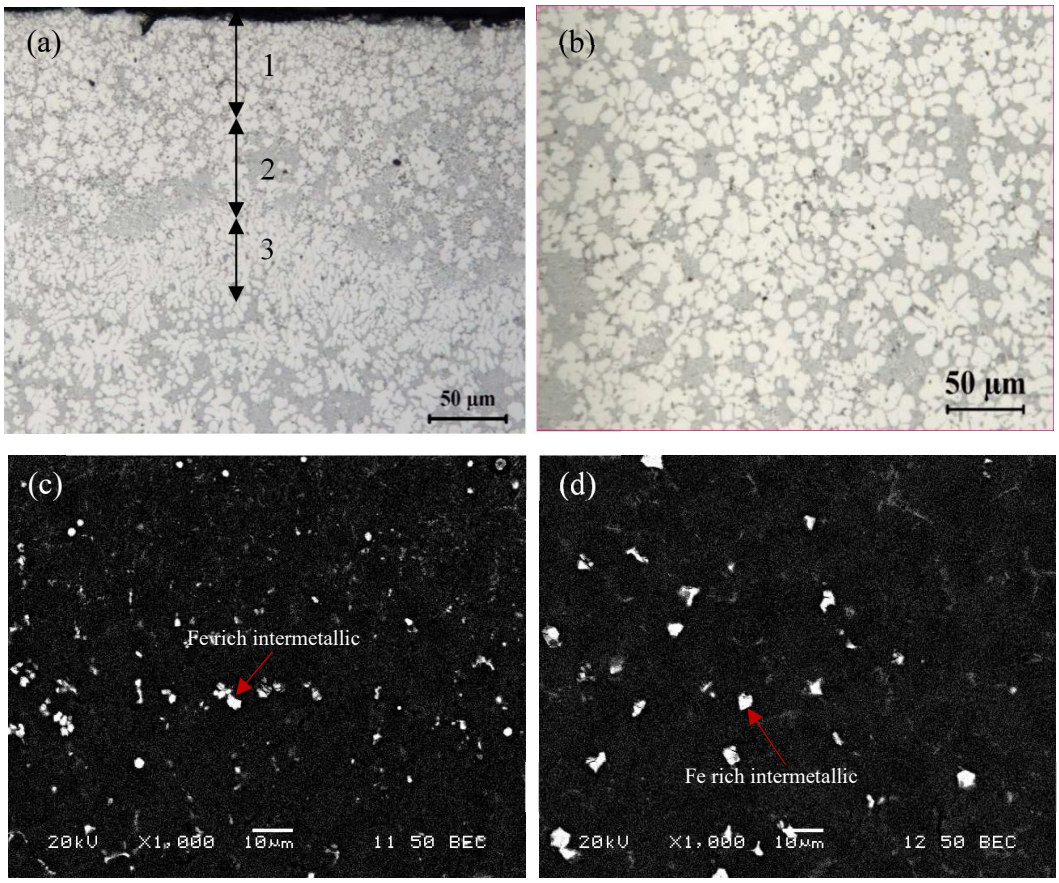

Figure 4.1: Microstructure of the as-cast HPVD sample: (a) optical images near cast surface (1. a skin sublayer; 2. a eutectic-rich sublayer, 3. an aluminum grain-rich sublayer), and (b) at the center; SEM electron backscattered images near (c) cast surface and (d) at the center.

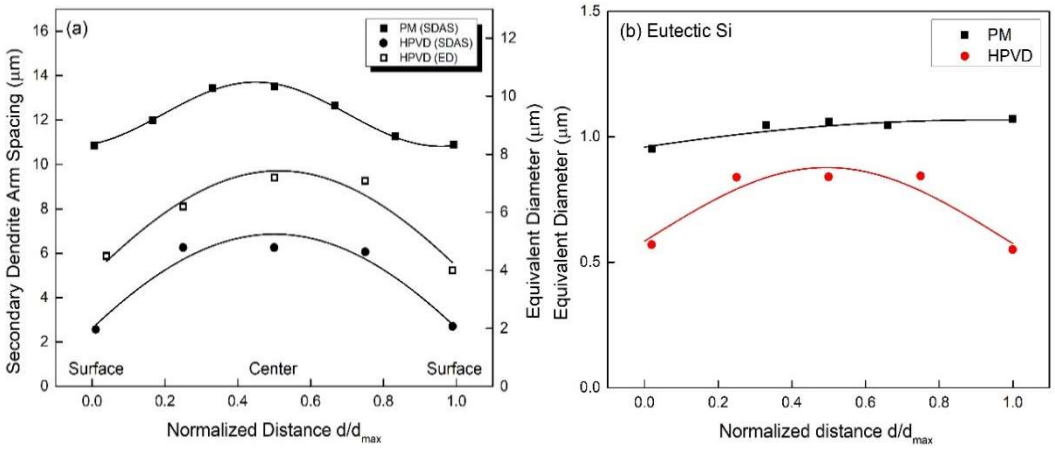

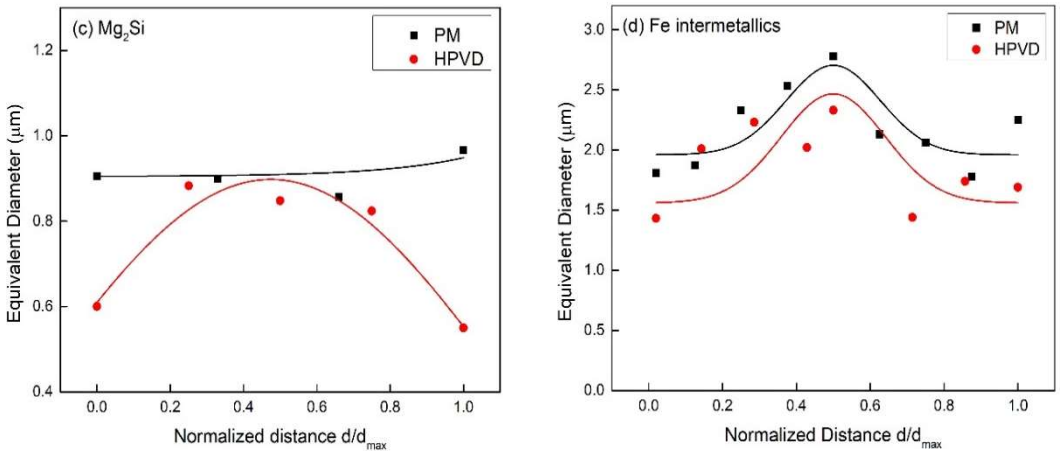

Figure 4.2: (a) The secondary dendrite arm spacing (SDAS) and equivalent diameter of aluminum grains; (b) the equivalent diameter of Si, (c) primary Mg_2Si and (d) Fe-rich intermetallics along the cross section of PM and HPVD samples. d: the distance from one edge to other; d_{max}: the sample thickness.

The microstructure of the PM sample near cast surface and at the center is shown in figure 4.3, which is composed of aluminum dendrite cells, Al-Si eutectic, primary Mg_2Si and Fe-rich intermetallic particles. The Fe-rich intermetallic particles have block shape near cast surface (figure 4.3 (c)) and the long needle-like morphology at the center (figure 4.3 (d)). The phases in PM samples are the same as those in HPVD samples. However, the morphology and size of those phases are greatly different in the two castings. The SDAS in the PM sample increases from the cast surface to the center but it is obviously larger than that in the HPVD sample (figure 4.2 (a)) due to a low cooling rate of PM casting. However, the SDAS variation of PM sample (from 8.2 μm at the surface to 10.5 μm in the center) is smaller than that of the HPVD sample (from 4 μm at the surface to 7 μm at the center). In general, the size of eutectic Si and primary Mg_2Si in the PM sample is greater than that in the HPVD sample (figure 4.2 (b)

and (c)). In addition, the size of eutectic Si and primary Mg_2Si almost does not vary along the PM sample cross section. Although the size of Fe-rich intermetallics in both PM and HPVD samples increases from the cast surface to the center, the average size of Fe-rich intermetallics in the PM sample is much larger than that in the HPVD sample (figure 4.3 (d) vs figure 4.1 (d)).

The Si and Mg distributions along the sample cross section in both HPVD and PM castings were investigated by EDS-SEM. The Si content in the surface layer of the HPVD sample (within 200-220 μm) varies remarkably (figure 4.4 (a)). In the skin sublayer, the Si content is lower than the average Si content (10.1 pct) in the alloy, whereas the Si in the eutectic-rich sublayer is much higher than that in the skin sublayer, followed a dramatic decrease in the Si content in the aluminum grain-rich sublayer. After the three sublayers, the Si content fluctuates between 10-11 pct in the distance from 0.3 mm to 1.0 mm. Further toward the sample center, the Si content decreases again. This indicates that there exists a macrosegregation of Si in the HPVD sample. Moreover, the Mg macrosegregation was also observed (figure 4.4 (b)). The Mg concentration in the cast surface (0-220 μm) is much higher than the average Mg content (0.55%) in the middle of the sample. After 1.0 mm, the Mg concentration decreases considerably toward the center. The macrosegregation of Si and Mg is attributed to the inverse segregation and exudation during the solidification under high pressure[2, 3]. On the other hand, there is no significant macrosegregation of Si and Mg in the PM sample. The Si content in the PM sample is fluctuated between 9-

11 pct (figure 4.4 (c) and Mg varies between 0.48% and 0.72% along the cross section (figure 4.4 (d)).

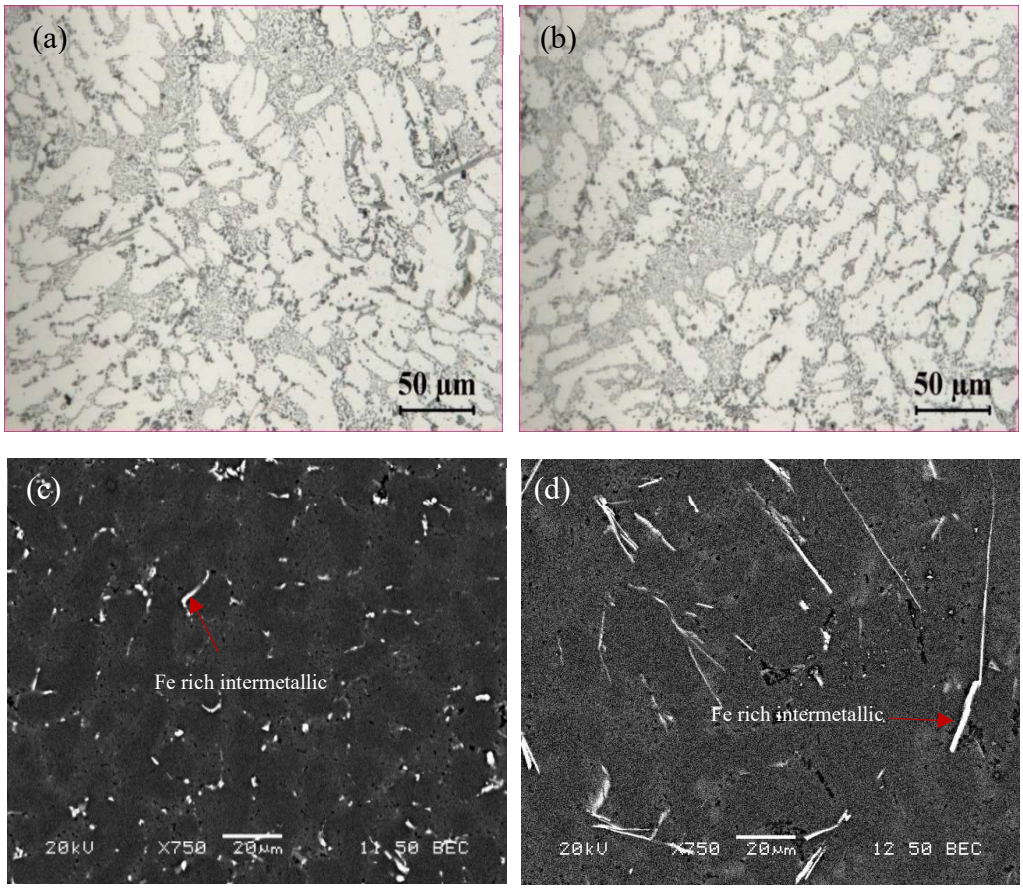

Figure 4.3: Microstructure of as-cast PM samples: optical images (a) near cast surface and (b) at the center; SEM electron backscattered image (c) near cast surface and (d) at the center.

Based on the quantitative image analysis results, it is interesting to find that the area fraction of primary Mg_2Si in the PM samples are 4 times higher than that in HPVD samples (0.21 vol.% in PM vs 0.05 vol.% in HPVD), although the Mg contents are similar in both samples (0.59% in PM and 0.55% in HPVD, see in Table 4.1). The measured electrical conductivity (EC) shows that the EC of PM samples is 34.35 %IACS but it is 29.87 %IACS in HPVD samples on as-

cast condition. This indicates that there are more solute Si and Mg supersaturated in the aluminum matrix of HPVD samples than that in PM samples.

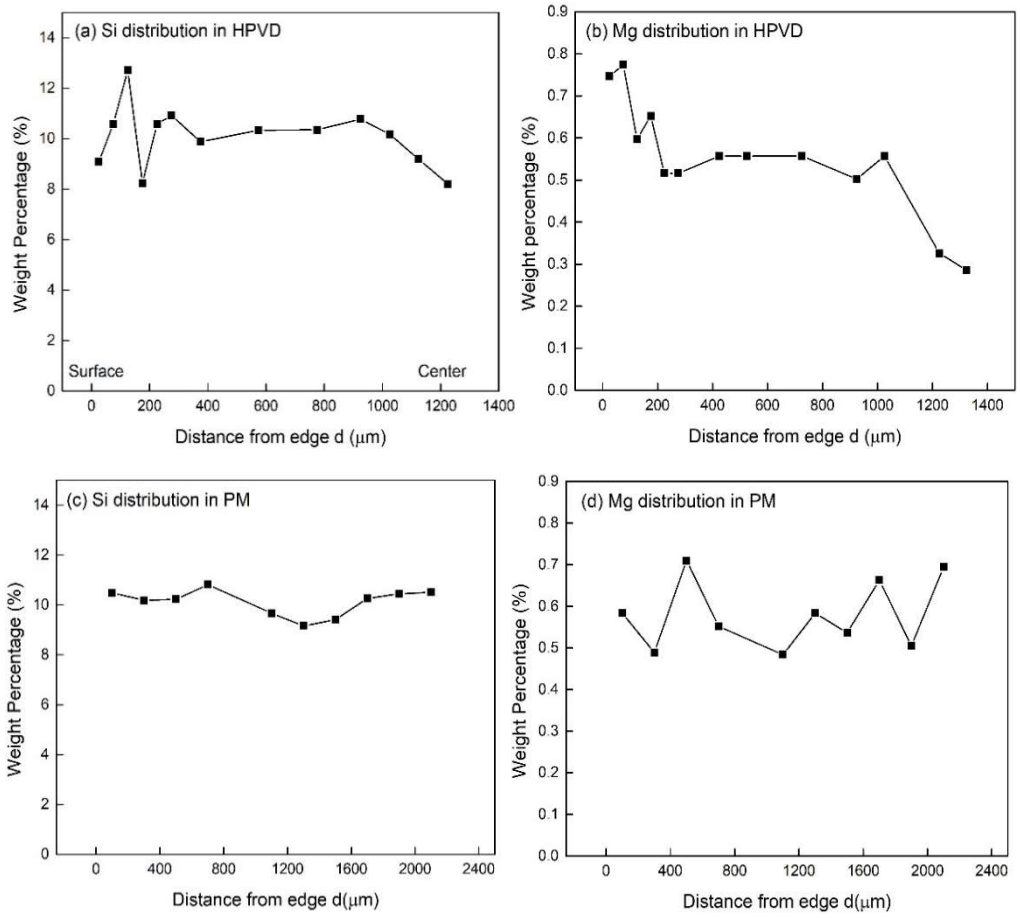

Figure 4.4: (a) Si (b) Mg distribution in the HPVD sample; (c) Si (d) Mg distribution in the PM sample.

Table 4.1: Chemical compositions of experimental alloys (wt.%)

Castings	Si	Mn	Mg	Ti	Sr	Fe	Al
PM	10.10	0.55	0.59	0.08	0.012	0.20	bal.
HPVD	10.10	0.55	0.55	0.08	0.011	0.18	bal.

Figure 4.5 shows the microstructure of HPVD and PM samples after T6 heat treatment. The plate-like eutectic Si on as-cast condition becomes more spherical after the T6 treatment in both samples (figure 4.5 (a) and (b)). However, the size

and morphology of the Fe-rich intermetallics in HPVD and PM samples does not change after T6 treatment. They are still dot- or rod-like morphology in the HPVD sample (figure 4.5 (c)) and the long needle-like shape in the PM sample (figure 4.5 (d)).

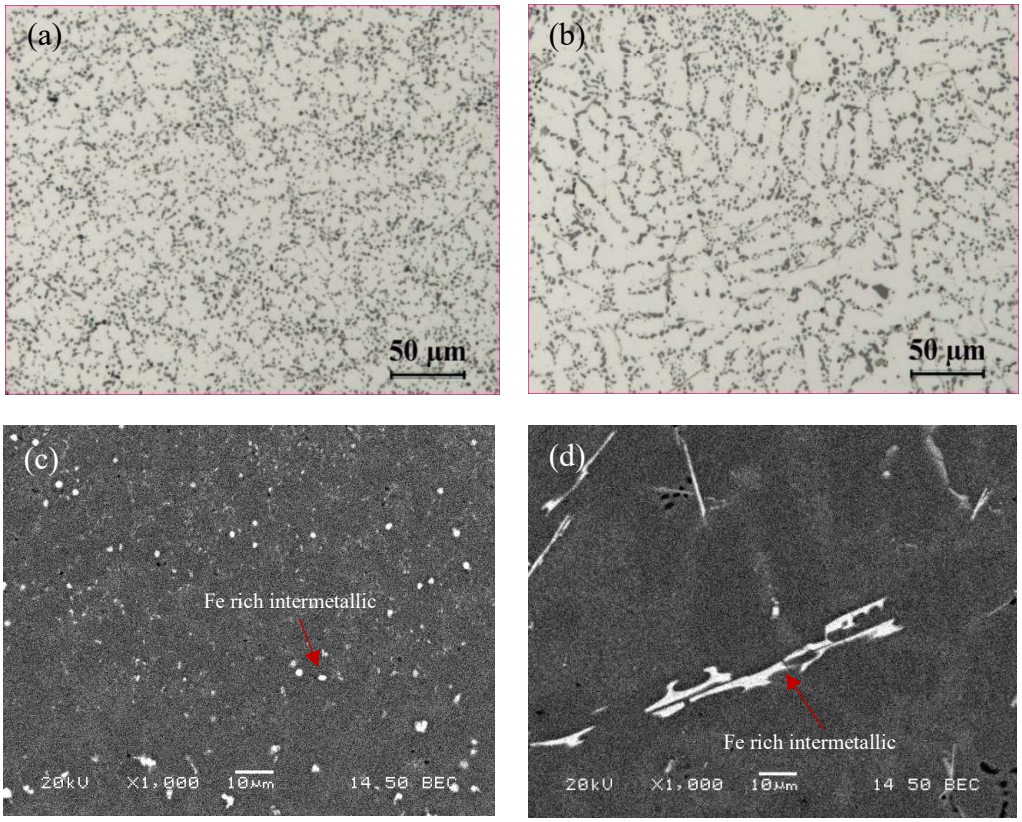

Figure 4.5: Microstructure in the sample center after T6 heat treated: optical images of (a) HPVD and (b) PM samples; SEM backscattered electron image of (c) HPVD and (d) PM samples.

4.1.2 Mechanical properties on as-cast condition and after T6 heat treatment

Figure 4.6 (a) shows the hardness profile along the cross section of HPVD and PM samples on the as-cast condition. The hardness near cast surface is considerably higher than that in the middle of the HPVD sample. For example,

the hardness is ~100 HV near cast surface but it is ~90 HV in the middle part of the sample. In the region near cast surface, the concentration of Si and Mg is higher than that in the middle part in the HPVD sample due to the macrosegregation (figure 4.4). The high hardness in the region near cast surface is mostly attributed to the solid solution strengthening. On the other hand, the hardness fluctuates between 85 HV to 88 HV along the cross section of the PM sample. The hardness variation along the cross section of the PM sample is small. The average hardness in the middle part of the HPVD sample is slightly higher than that in the PM sample.

The tensile properties of HPVD and PM samples on the as-cast condition are shown in figure 4.6 (b). It is evident that the tensile properties of HPVD castings are remarkable better than those of PM castings. The YS of the PM sample is approximately 68% of that of the HPVD sample while the UTS of the former is approximately 57% of that of the latter. Particularly, the elongation of the PM casting is quite low and only 21% of that of the HPVD casting, which is most likely related to the long needle-like Fe-rich intermetallic in the PM casting.

Figure 4.7 (a) showed the hardness profile along the cross section of HPVD and PM samples after T6 heat treatment. The hardness near the cast surface of two castings is slightly higher than that at the sample center. The hardness of the HPVD sample varies between 112 HV and 117 HV. Compared to the as-cast condition, the hardness difference between the surface and center after T6 is smaller, which would be attributed to the disappearance of solute supersaturation at the near surface region. On the other hand, the hardness of the

PM sample varies between 117 HV and 121 HV. It is interesting to note that the hardness of the PM sample is higher than that of HPVD samples on the T6 condition. The hardness increases in PM and HPVD samples are 38% and 24% respectively, relative to the hardness on the as-cast condition. In other words, the effect of the T6 treatment on the hardness improvement is more predominant in the PM sample.

Figure 4.7(b) shows the tensile results of HPVD and PM samples on the T6 condition. For HPVD castings, the YS after T6 reaches 175 MPa, which is an approximate 3% increase over the as-cast condition. The UTS is only 257 MPa, which is an approximate 20% decrease compared to the as-cast condition. The elongation of the HPVD sample increases from 8% on as-cast condition to 10% after T6. It seems that the T6 treatment can only improve the elongation of HPVD castings, but it has limited impact on the tensile strength. For PM castings, the YS and UTS reach 183 MPa and 247 MPa respectively, which present a 59% increase in YS and a 35% increase in UTS over that on the as-cast condition. It is evident that the T6 treatment greatly improves the tensile strength of PM castings. After T6 heat treatment, the tensile strength of PM castings can reach the similar level of HPVD castings. However, the elongation of PM castings is always much lower than that of HPVD castings on both as-cast and T6 conditions.

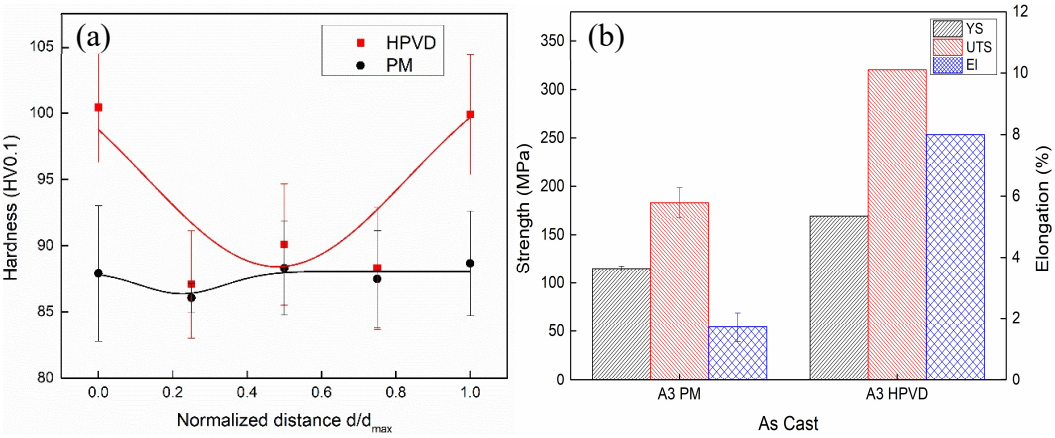

Figure 4.6: Mechanical properties of HPVD and PM samples on as-cast condition: (a) the hardness profile along the cross section and (b) the tensile properties. Tensile properties of HPVD are taken from Breton and Fourmann (2016)[25]. d: the distance from one edge to other; d_{max}: the sample thickness.

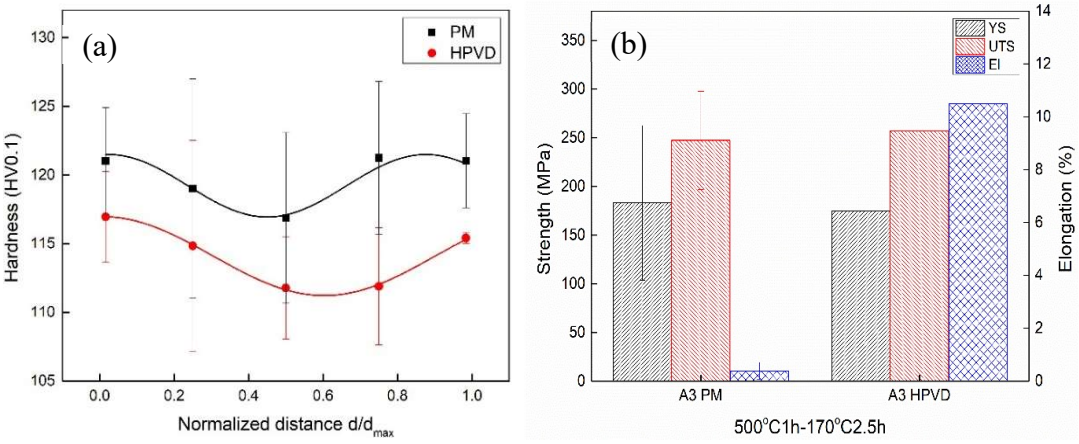

Figure 4.7: Mechanical properties of HPVD and PM samples on T6-treated condition: (a) the hardness profile along the cross section and (b) the tensile propertie. Tensile properties of HPVD are taken from are taken from Ref.15. d: the distance from one edge to other; d_{max}: the sample thickness.

4.1.3 Summary

(1) In the high pressure vacuum die (HPVD) casting, there exists a surface layer that has a unique feature and different structures. The surface layer can be divided into 1) a skin sublayer directly adjacent to the cast surface, 2) a eutectic-

rich sublayer next to the skin sublayer and followed by 3) an aluminum grain-rich sublayer.

(2) The macrosegregation of Si and Mg in the cross section of as-cast HPVD samples has been observed. In general, the Si and Mg concentrations are enriched in the surface layer and depleted in the center of the sample. On the other hand, there is no significant macrosegregation of Si and Mg in the permanent mold (PM) samples.

(3) The microstructure of PM samples is composed of the same phases as those of HPVD samples. The dimension variation of microstructural phases along the cross section in PM samples is less than that in HPVD samples, although the size of microstructural phases in PM samples is much larger than that in HPVD samples.

(4) The hardness near the cast surface is considerably higher than that in the middle of as-cast HPVD samples. The hardness in the middle part of the HPVD sample is slightly higher than that in the PM sample on the as-cast condition. However, after T6 heat treatment the hardness of the HPVD sample is lower than that of the PM sample.

(5) The tensile properties of HPVD castings are remarkable better than those of PM castings on the as-cast condition. The T6 heat treatment greatly improves the tensile strength of PM castings while it has limited impact on the tensile strength of HPVD castings. After T6 treatment, the tensile strength of PM castings can reach the similar level of HPVD castings.

4.2 Quench sensitivity of Aural™ 3 HPVD and PM

4.2.1 Time-temperature-transformation curves

The evolution of electrical conductivity (EC) is correlated to the phase transformation during isothermal process because more solute atoms transformed into precipitates results in a lower electrical conductivity of a sample. The electrical conductivity evolutions of the solution heat treated HPVD and PM after isothermal treatment are shown in Fig. 4.8(a) and Fig. 4.9(a), respectively.

Generally, the electrical conductivity increases with the extension of the isothermal holding time. The augmentation of electrical conductivity is fast at the beginning of the isothermal holding period. Then the rate of increase slows down, before it eventually reaches a stable value. When the isothermal treatment at 375°C, the increasing rate of the EC of HPVD is faster than that at other temperatures as shown in Fig. 4.8(a), whereas the fastest EC increasing rate is at 350°C for PM (Fig. 4.9(a)). For HPVD, the electrical conductivity of solution treated sample is 37.0% IACS, which represents a supersaturated solid solution state. The conductivity of isothermal holding at 375°C for 27h is 42.95% IACS. It responses a complete decomposition of supersaturated solid solution. For PM, the electrical conductivity of solution treated sample is 36.3% IACS, while the conductivity of isothermal holding at 350°C for 27h is 42.40% IACS.

The measured percentages (10 to 40) of the conductivity difference between the supersaturated solid solution and a complete decomposition of supersaturated solid solution were used to determine the temperature-time-

transformation (TTT) curves, as shown in Fig. 4.8(b) and Fig. 4.9(b). The percentage of the phase transformation in the TTT curves is corresponding to the electrical conductivity variation in Fig. 4.8(a) and Fig. 4.9(a), respectively. The TTT curves possess ‘‘c’’ shapes. The nose temperature of HPVD is 375°C. The critical time, which is the incubation of 10% precipitates at nose temperature, is 10 seconds. The quench sensitivity temperature range is 275-450 °C. In the range, electrical conductivity decreases quickly, but outside of the range, electrical conductivity decreases slowly as holding time extends. In other words, the rate of phase transformation is fast in this temperature range.

For PM, the nose temperature is 350°C, which is lower than HPVD. The quench sensitivity temperature range is 255-430°C. The PM quench sensitivity temperature range is in a lower temperature range than that of HPVD. The critical time for 10% precipitate transformation is 14s, which is 40% longer than HPVD (10s). Hence, HPVD has a shorter critical time, a higher nose temperature, and a slightly higher quench sensitivity temperature ranger than PM.

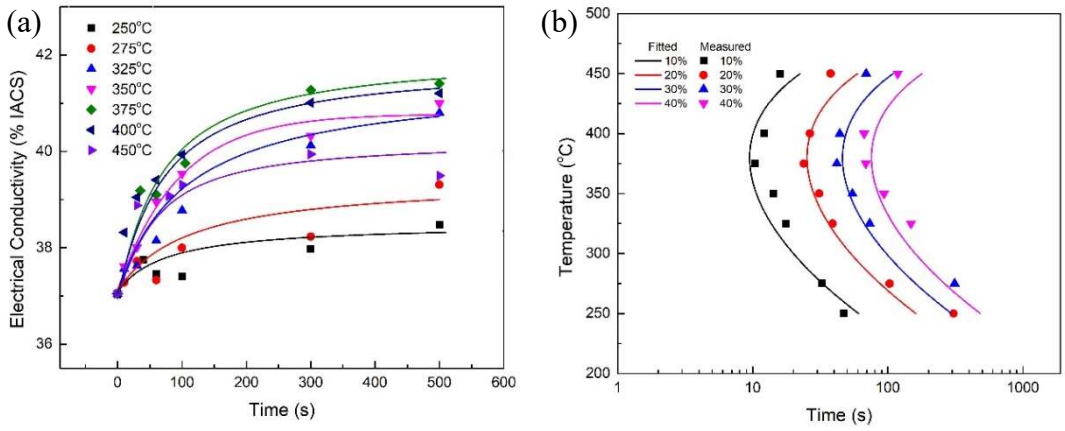

Figure 4.8: (a) Effect of isothermal treatment on conductivity of as-quenched HPVD samples (b) TTT curve of HPVD samples.

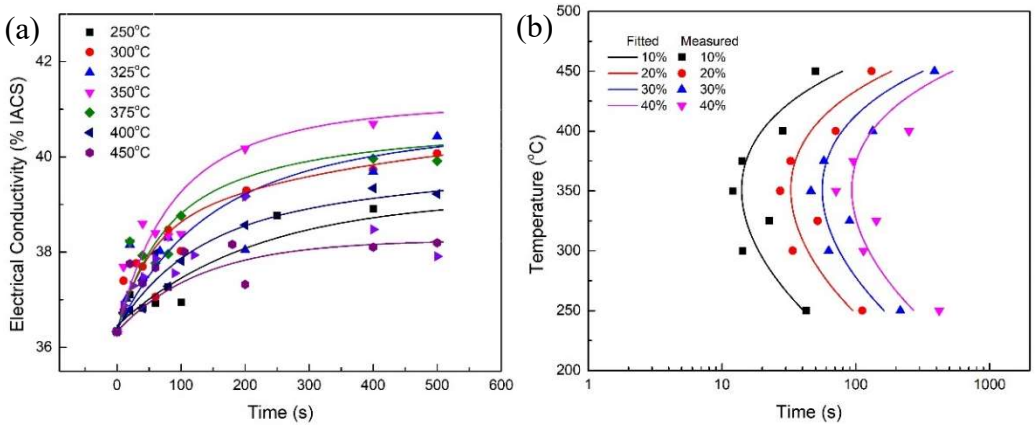

Figure 4.9: Effect of isothermal treatment on electrical conductivity of as-quenched PM (a), TTT curve of PM (b).

4.2.2 Time-temperature-properties curves and quench factors

It was well known that the mechanical property of aluminum alloys varies with the evolution of precipitation in heat treatment. The Vickers hardness of HPVD, solution treated at 500°C for 3 hours and then aged at 175ºC for 2.5 h, is 120HV, while it is 125HV for PM. Figs. 4.10 (a) and 4.11 (a) illustrates the hardness evolution in the isothermal treatments at various temperature and holding time. Generally, the hardness decreases with the extension of the isothermal holding time. However, the hardness drop rate at 375ºC is faster than that at other temperatures for HPVD (Fig. 4.10 (a)). Meanwhile, the temperature with the fastest hardness drop is 350ºC for PM (Fig. 4.11(a)).

The measured hardness, 99.5 to 80% of the maximum hardness, of the isothermal treated samples were used to determine the TTP curves based on the Eq. (2.3).

TTP curves of HPVD and PM samples with 99.5%, 95%, 90%, and 80% of the maximum performance were described as shown in the Fig. 4.10 (b) and Fig. 4.11 (b), respectively. The TTP curves present ‘‘c’’ shape. The nose temperature of HPVD is about 375^{o}C, and it is near 350^{o}C for PM (Figs. 4.10 (b) and 4.11 (b)). The TTP nose temperatures of the HPVD and PM are similar to those in TTT curves, respectively (Fig. 4.8). The quench sensitivity temperature range of the former is 275^{o}C-450^{o}C, while it is from 255^{o}C to 430^{o}C for the latter. In the temperature ranges, the hardness drop is faster than that out of this temperature ranges.

The TTP curves of 99.5% and 80% of the maximum hardness values are illustrated in Fig. 4.12, respectively, to compare the quench sensitivity of HPVD and PM. It is clear that the expended time required to obtain 99.5% or 80% of the maximum hardness for HPVD samples is shorter than that for PM samples especially when the temperatures is higher than 300°C. As temperatures increase, there is a corresponding increase in the gap of the time to obtain 99.5% or 80% maximum hardness between the two types of samples. At nose temperature, the critical time needed to achieve 80% and 99.5% maximum hardness is 0.6s and 14s respectively for HPVD, while the corresponding levels for PM require 0.8s and 20s respectively. Therefore, the HPVD have a higher nose temperature and shorter critical time than PM, which indicate that the precipitation in the former is faster than the latter. On the other words, the quench sensitivity of HPVD is higher than that of PM.

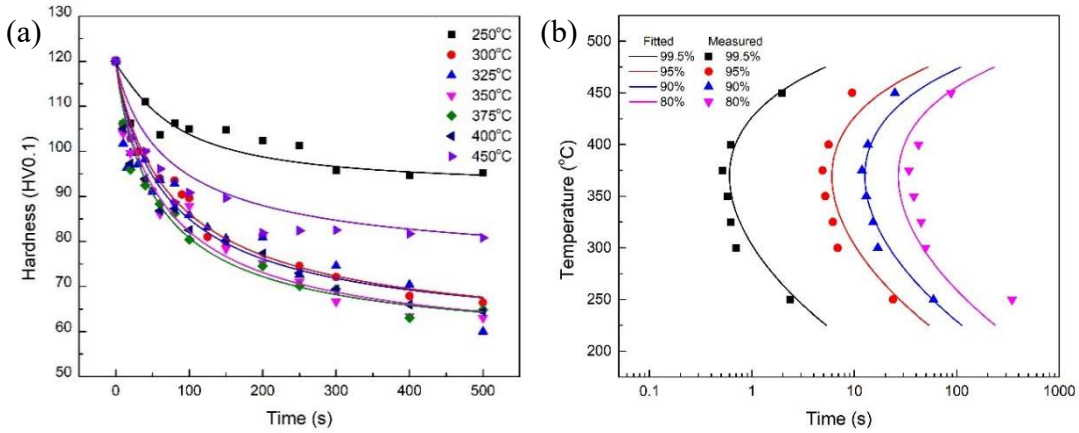

Figure 4.10: Effect of isothermal treatment on hardness (a), and TTP curves (b) of Aural™-3 HPVD.

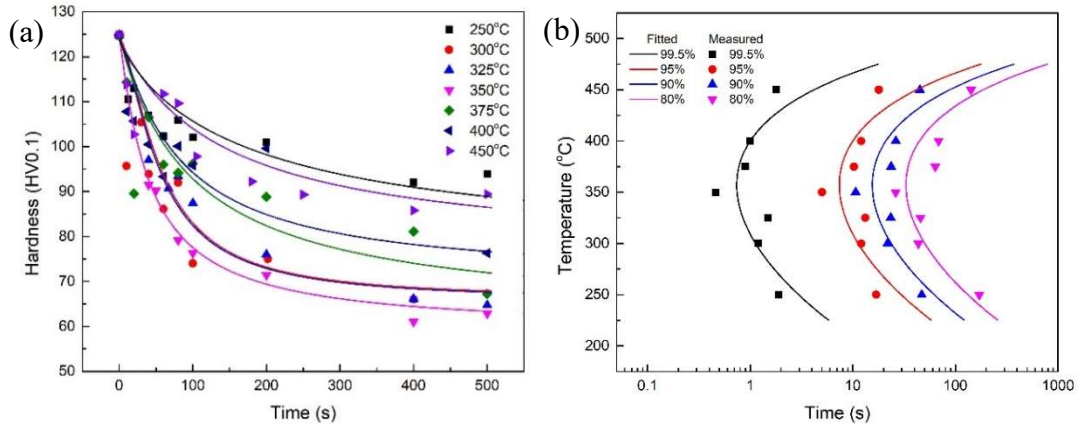

Figure 4.11 : Effect of isothermal treatment on hardness (a), and TTP curve (b) of Aural™-3 PM.

Table 4.2 : Coefficients for TTP diagram of Aural™-3 HPVD and PM.

	k2	k3	k4	k5
Aural™-3 PM	0.35×10^{-6}	3103	955	77243
Aural™-3 HPVD	1.92×10^{-6}	2483	955	72966

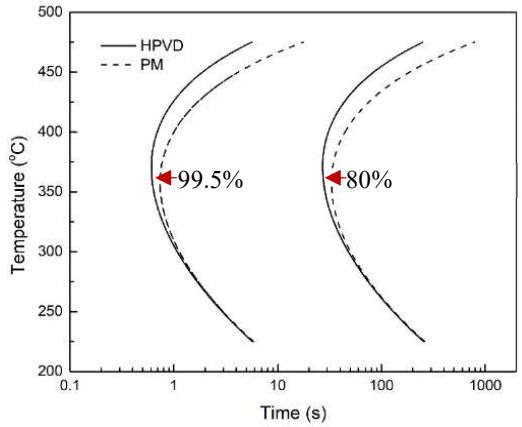

Figure 4.12 : TTP curves of 99.5% and 80% of maximum hardness of Aural™-3 HPVD (solid) and Aural™-3 PM (dash).

The coefficients in the equation (2.3) were determined by non-linear least squares and fitting with the measured results, given in the Table 4.2. It can be seen that k2, constant associated with the reciprocal of the number of nucleation sites, in HPVD is slightly higher than that in PM, which means that the number of active nucleation sites in HPVD would be less than that in PM. K3 in HPVD is slightly less than that in PM, which indicates that energy required to generate nucleus in HPVD is less than that in PM. The k4 values, related to the solvus temperature, are the same owing to the similar chemical compositions of the two samples. The value of K5 of HPVD is a little lower than that of PM, which indicates that the solute in HPVD is likely to diffuse more readily than that in PM.

Quench factor analysis has been used as a mathematic method to study the continuous quenching process by using isothermal heating tests.

Quench factor, τ, can be calculated according to the equation (4.1)[15] below.

$$\tau = \sum_{t_o}^{t_f} \frac{\Delta t}{C_t(T)} \quad \text{.....(4.1)}^{15}$$

Where

$C_t(T)$ is the critical time for a certain amount of solute to precipitate as shown in TTP curves;

t_o is the time at the start of the quench;

t_f is the time at the end of the quench.

The relationship between quench rate and mechanical properties then could be determined based on quench factor analysis method. The predicted strength, σ, would be expressed as equation (4.2)[15]:

$$\sigma = \sigma_{max} \exp(k_1 \tau) \ldots\ldots\ldots\ldots\ldots\ldots\ldots\ldots\ldots\ldots (4.2)^{15}$$

Where σ_{max} is the maximum property attainable with an infinite quench rate.

And, then, the properties drop can be determined by equation (4.3)[15].

$$\Delta\% = 1 - \exp(k_1 \tau) \ldots\ldots\ldots\ldots\ldots\ldots\ldots\ldots\ldots\ldots (4.3)^{15}$$

Where Δ is the hardness drop;

k_1 and τ were taken from the equation (4.1) and (4.2).

To ensure the accuracy of the calculated results, Δt=0.1s in equation 2 has been selected because the temperature drop during each time step should be less than 25°C[51]. In addition, the temperature range of 250-450°C is used for the quench factor calculation because when the quench sensitivity temperature range, 275-450°C for HPVD and 255-430°C for PM in TTP curves, is included for the calculation, the effect of temperature range on quench factor is ignored [52]. The effect of the cooling rate from 2 to 200°C/s through selected temperature ranges of the experimental samples on quench factor, predicted hardness and hardness drop was inspected, as shown in Fig. 4.13 and 4.14.

Figure 4.13 (a) illustrated the effect of cooling rates on quench factor and predicted hardness of HPVD. It is clear that with increasing cooling rate, quench factor decreases and the predicted hardness increases. The quench factor decreases rapidly until it reaches a certain cooling rate, C_r. When the cooling rate is higher than C_r, the variation of the quench factor and predicted hardness becomes small. C_r of HPVD is determined as 20°C/s according to Fig. 4.13 (a). Fig. 4.13 (b) demonstrates the relationship between cooling rate and hardness drop in HPVD. The hardness drop decreases with the cooling rate increasing. The change of hardness drop becomes slow when the cooling rate is higher than C_r, 20°C/s. At 20°C/s, the hardness drop of HPVD is 5% of the maximum hardness. On the other words, as the cooling rate is higher than 20°C/, more than 95% of maximum hardness can be obtained for HPVD. The effect of cooling rates on quench factor, hardness, and hardness drop of PM are qualitatively similar to that of HPVD samples, shown in Fig.4.14. The C_r of PM is 17°C/s. As the cooling rate is higher than 17°C/, more than 95% of maximum hardness can be obtained for PM (Fig. 4.14 (b)). The red dots in Fig.4.13 (b) and Fig.4.14 (b) are the results obtained from the experiments, and the black lines are the predicted hardness drop based on equation (4.3). We can see that the predicted results agree well with experimental hardness. Therefore, HPVD needs higher cooling rate than PM to obtain the same percentage of maximum hardness. It is another evidence that HPVD is more quench sensitive than PM.

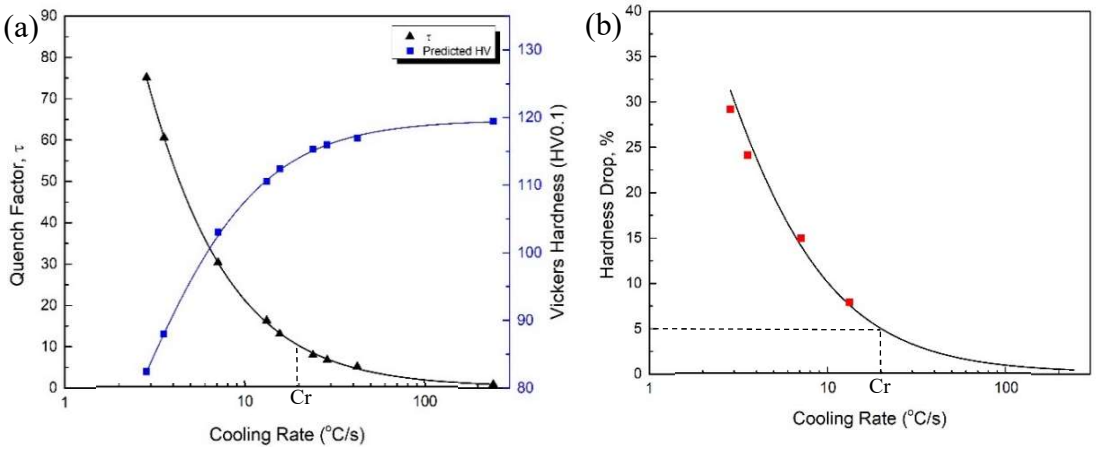

Figure 4.13 : Effect of cooling rate on quench factor and predicted hardness (a), and on hardness drop (b) of HPVD.

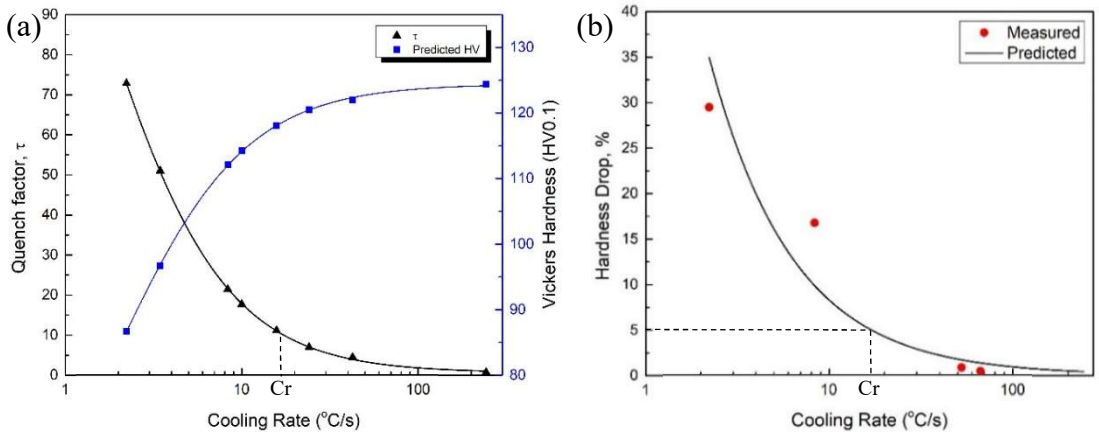

Figure 4.14 Effect of cooling rate on quench factor and predicted hardness (a), and on hardness drop (b) of PM.

4.2.3 Differential scanning calorimetry

Non-isothermal DSC analysis of solution treated samples is typically used to investigate the precipitation kinetics of strengthening phases. Fig. 4.15 demonstrates the DSC heating curves of solution treated HPVD and PM with a heating rate, 10°C/min. The heating curves reveal three exothermic peaks, A, B and C, in HPVD and PM respectively. Table 4.3 lists the average data related to

the peaks. According to Table 4.3, the temperature of onset and peak of peak A of HPVD is 214°C and 243°C, and the PM have almost the same values for the peak A. However, as we can see, the onset and peak temperature of peak B of HPVD are 360°C and 405°C, respectively, which are lower than those (413°C and 434°C, respectively) of PM. Moreover, the onset and peak temperature of peak C of HPVD are situated at 453°C and 498°C, respectively, which also are lower than those (485°C and 502°C, respectively) of PM. Peak A, B and C represent the precipitation of β'', β' and β, respectively, according to the reference[53]. Thus, the precipitation of β' and β in HPVD occurred at a lower temperature than that in PM, which indicates that the precipitation of β' and β in HPVD is easier than that in PM.

It should also be noted that an aging temperature of 170 ºC was chosen, lower than peak temperature of β''. Because that DSC tests are continuous fast heating process rather than aging which is an isothermal heating process. In the DSC continuous heating test at 170 ºC, it needed long phase transformation time because of low diffusion coefficient. So β'' would require additional time to precipitate. However, aging should be considered as extremely slow heating at 170ºC for 2.5h. This allows enough time for β'' to precipitate, even at a low diffusion rate.

(a)

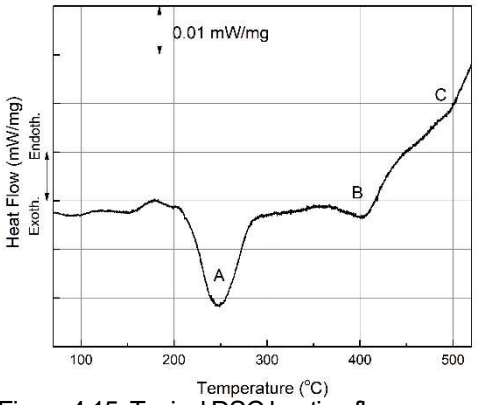

(b)

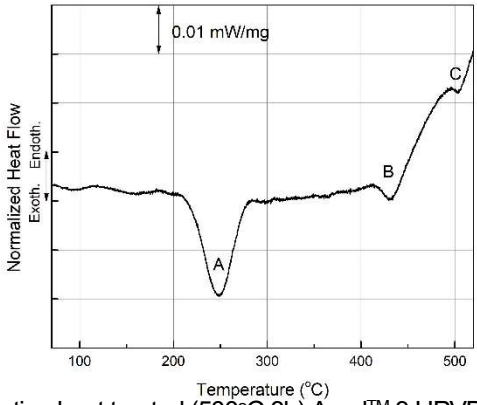

Figure 4.15: Typical DSC heating flow curves of solution heat treated (500°C 3h) Aural™ 3 HPVD (a), Aural™ 3 PM (b).

Table 4.3 : Average values of onset and peak temperature of HPVD and PM.

	Peak A		Peak B		Peak C	
Castings	Onset T (°C)	Peak T(°C)	Onset T (°C)	Peak T (°C)	Onset T(°C)	Peak T (°C)
Aural™-3 HPVD	214	243.50	360	405	453	498
Aural™-3 PM	214	243.10	413	434	485	502

4.2.4 Microstructure observation

The microstructure of solution heat treated HPVD is composed of Al grains, block-like Fe rich intermetallic, and fine and fibrous-like Si phases, as well as small amount of Mg_2Si particles, as shown in Fig. 4.16 (a). On the other side, Al dendrite cells, plate-like Fe rich intermetallic phase, plate-like Si, and small amount of Mg_2Si particles were observed in PM, as indicated in the Fig. 4.16 (b). Generally, the types of phases in HPVD is similar to that in PM, but the size of the phases in the former are much smaller than in the latter. Fig. 4.17 illustrates the EBSD mappings of HPVD and PM respectively, the black lines indicate the grain boundaries (misorientation more than 15 degrees). Table 4.4 shows the

statistical data of grain size and the length of grain boundaries in HPVD and PM. It is clear that the average equivalent grain diameter in HPVD is much smaller than that in PM samples. The latter is around 22 times to the former. And the grain boundary in HPVD is 15 times longer than that in PM.

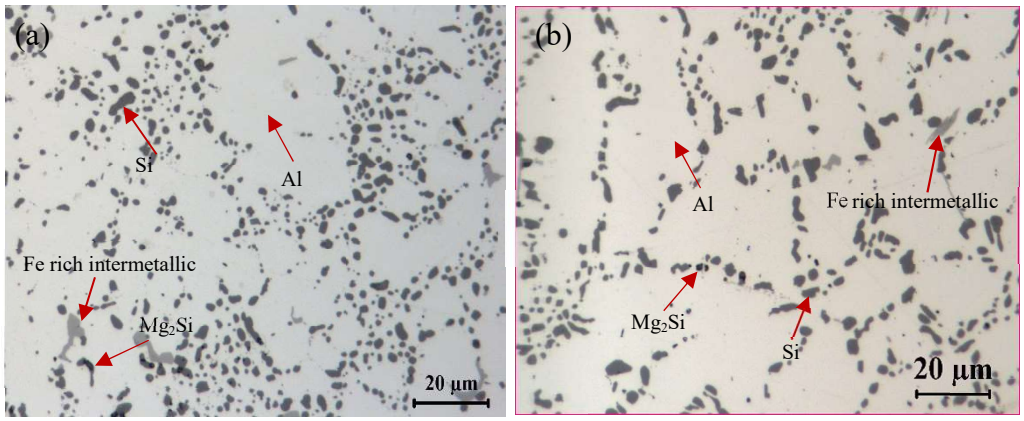

Figure 4.16 : optical microstructure of solution heated (500°C for 3h) Aural™ 3 HPVD (a), and Aural™ 3 PM (b).

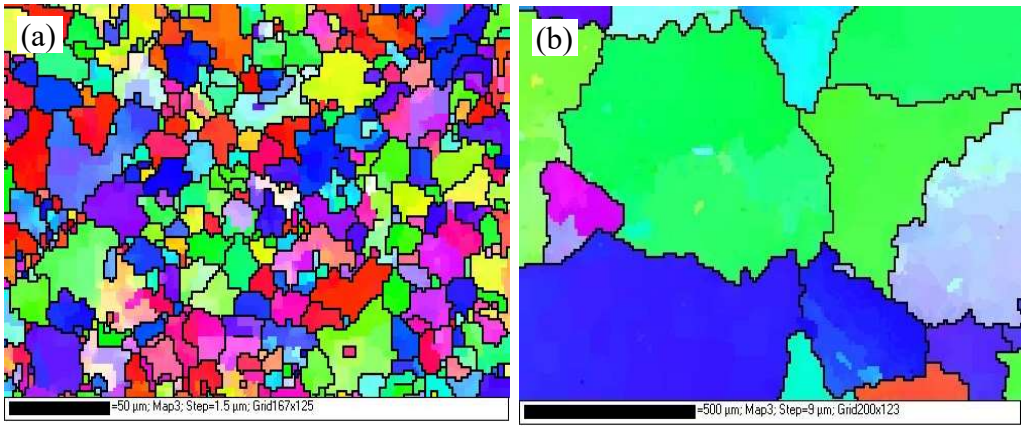

Figure 4.17 : EBSD mappings of solution treated HPVD (a), and PM (b). Dark lines indicate that the misorientation is more than 15 degrees.

Table 4.4 : Grain size and grain boundary length of Aural™ 3 HPVD and PM

	Grain diameter (µm)		Grain boundary length per μm^2 ($\mu m/\mu m^2$)	
Samples	Average	STD	Average	STD
HPVD	4.4	3.5	11.28	0.71
PM	95.2	40.2	0.67	0.18

The precipitates in aluminum matrix and along grain boundary in HPVD and PM at nose temperature or on as-aged condition are shown in Figs. 4.18-4.20. The needle-like Mg_2Si precipitates with 20−50 nm in length, which would be β''-Mg_2Si phase according their dimension[54], uniformly exhibit in the aluminum matrix of as aged HPVD and PM, respectively, in Fig. 4.19 (a) and (b).

The precipitates in HPVD and PM at nose temperature of TTP curves were examined to understand the precipitation during isothermal heat treatment. In HPVD, when isothermal heat treated at nose temperature, 375°C for 300 seconds, few rod-like Mg_2Si phases with a length of 1-2μm and thickness of 15-25 nm were observed in aluminum matrix, which would be β-Mg_2Si phase[54], as shown in Fig. 4.19 (a), meanwhile, many granular-like Mg_2Si particles with a diameter of 0.5-2μm along grain boundary were found (Fig. 4.19 (b)). On the other side, many rod-like β-Mg_2Si phase with a length of 1-3μm and a thickness with around 20-50nm were observed in PM, as shown in Fig. 4.20. It is worth mentioning that Mn-containing dispersoids were observed and some of rod-like β-Mg_2Si particles attached on the dispersoids in PM (Fig. 4.20). These Mn-containing dispersoids would act as nucleation sites in favour of precipitate nucleation. The amount of Mn-containing dispersoids in PM is much more than that in HPVD.

Therefore, at nose temperature, the precipitates mainly generate along grain boundaries for HPVD, while the rod-like β-Mg_2Si phases mainly precipitate in aluminum matrix in PM.

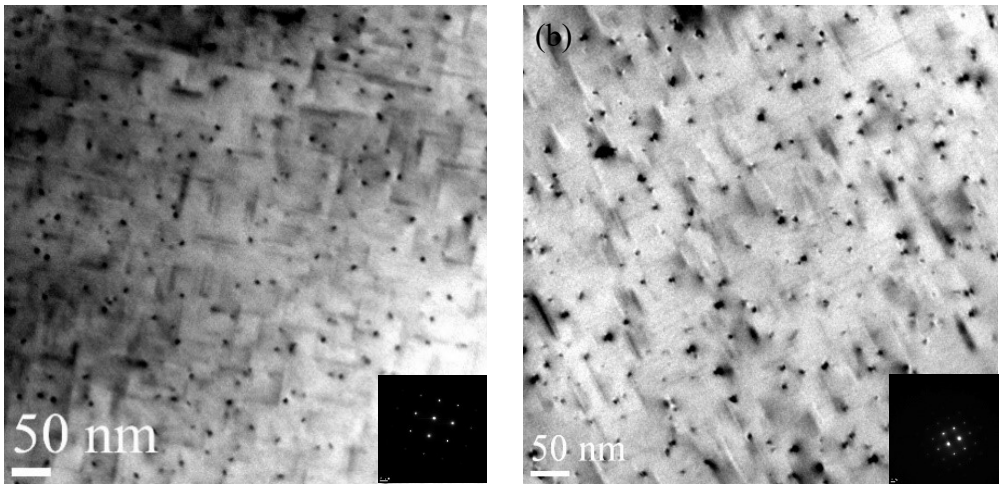

Figure 4.18: BF TEM images of precipitates in as-aged HPVD (a), and PM (b), recorded near $[001]_{\alpha\text{-Al}}$ direction. The insets in (a) and (b) are the SAD patterns at $[001]_{\alpha\text{-Al}}$ direction.

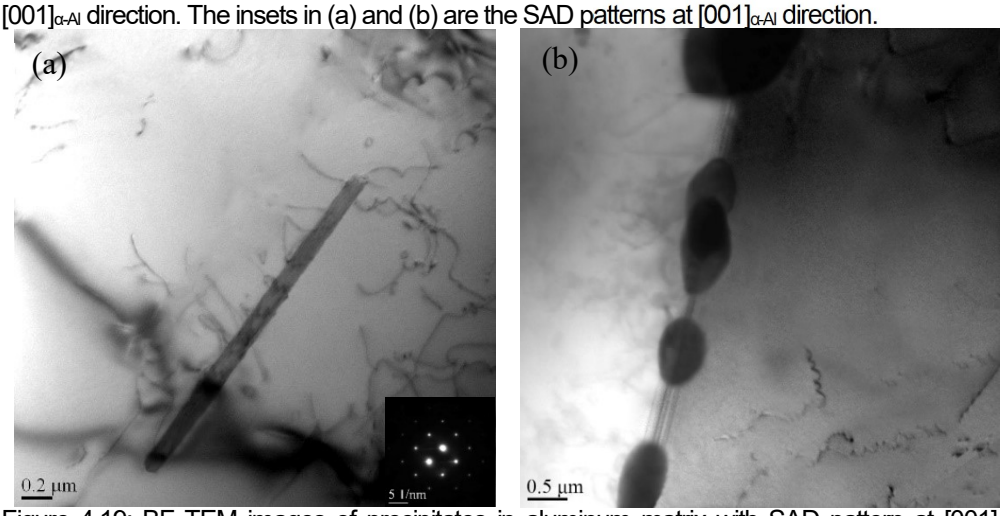

Figure 4.19: BF TEM images of precipitates in aluminum matrix with SAD pattern at $[001]_{\alpha\text{-Al}}$ direction (a) and grain boundary of HPVD (b), isothermal treated at nose temperature for 300s, recorded near [001] direction.

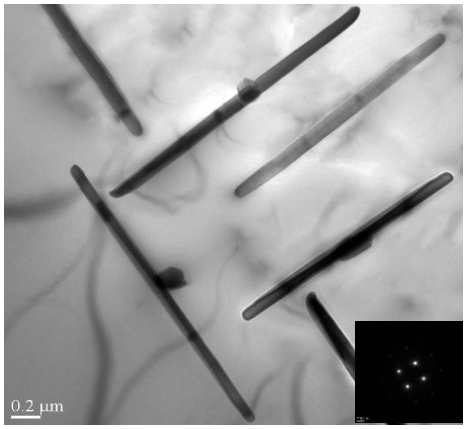

Figure 4.20: TEM images of Aural™ 3 PM quenched specimens held at 360 °C for 300 s with SAD pattern. The inset is the SAD pattern at $[001]_{\alpha\text{-Al}}$ direction.

4.2.5 Discussion

When the isothermal holding temperature is higher than nose temperature, the precipitation is controlled by phase nucleation because the driving force for precipitation is low[38]. Hence, grain boundaries or other suitable particles would become preferred locations for heterogeneous nucleation of phases during heat treatment at high temperature, due to their low energy required for nucleation [38]. HPVD have much finer grain size along with much longer grain boundaries than PM (see Table 4.4). On the other side, there are more Mn-containing dispersoids in PM than HPVD at nose temperature (see Figs. 4.19 and 4.20). The value of k_2, calculated coefficient, from TTP curves in HPVD is smaller than that in PM (see Table 4.2). It implies that HPVD would have less active nucleation sites than PM, which could be due to larger amount of Mn dispersoids in PM. These dispersoids could provide more potential nucleation sites than grain boundaries in HPVD. However, lower k_3 and k_5 values in HPVD than that in PM (see Table 4.2) indicate that less energy requires to form a nucleus on grain boundaries in HPVD than on substrates like Mn-containing dispersoids in PM, attributed to the fact that the precipitates mainly nucleate and glow along grain boundaries in HPVD at temperature higher than nose temperature, rather than on dispersoids at aluminum matrix as in PM. The DSC analysis results also demonstrate that the precipitation of β' and β in HPVD is easier than that in PM (see Table 4.3). As we can see from the Fig. 4.19 (b), the granular-like Mg_2Si particles along grain boundaries in HPVD has larger volume than needle-like Mg_2Si on the matrix in PM. Thus, the precipitation of Mg_2Si phases in HPVD is easier and

growth is faster than that in PM, consequently, which results in a shorter critical time of the precipitation in HPVD than that in PM at nose temperature of TTT and TTP curves, respectively. Therefore, the quench sensitivity of HPVD is higher than that of PM.

When the heat treatment is at 170°C, which is much lower than that nose temperature of TTP curves, precipitation is controlled by solute diffusion. According to diffusion length in metal, L, equation (4.4) [14]:

$$L = \sqrt{Dt} \quad \text{.....(4.4)}^{14}$$

Where

L is the diffusion length in meters

D is the diffusivity in m^2/s

t is the diffusion time

Magnesium is the one of the main elements in Mg_2Si precipitates. The calculated diffusion length of magnesium solute based on equation 5 is 31 nm using D = 1.07×10^{-19} m^2/s, diffusion coefficient of Mg in aluminum at 443 K (170°C)[55] and t = 9000s (2.5 hours). The diffusion length is much shorter than the grain size of HPVD (4.4μm) and PM samples (95.2 μm). Therefore, fine and uniform precipitates, β''-Mg_2Si, appear at aluminum matrix in both HPVD and PM samples (see Fig. 4.18) at low temperature, which agrees with DSC analysis results: the onset and peak temperature of β''-Mg_2Si in HPVD are the almost same as those in PM (see Table 4.3).

4.2.6 Summary

1. The TTP and TTT curves of HPVD and PM of Al-10Si-0.5Mg alloy have been constructed. The quench sensitivity temperature range of HPVD is from 275 ºC to 450 ºC, and its nose temperature is 375ºC, while the nose temperature of PM is 350ºC and its sensitivity temperature range is from 255 ºC to 430 ºC. HPVD has shorter critical time for 10% precipitate transformation and to obtain 99.5% of maximum hardness than PM. HPVD has higher quench sensitivity than PM.

2. The cooling rate for HPVD has to be higher than 20℃/s, but for PM, it should be higher than 17℃/ to obtain more than 95% of maximum mechanical performance.

3. The casting processes have an impact on the quench sensitivity mainly due to the discrepancy of their microstructures. At nose temperature, Mg_2Si precipitates are more likely to nucleate and grow along grain boundary in HPVD, but they prefer to distribute in the aluminum matrix in PM.

4.3 The quench sensitivity of Aural™ 5 HPVD

4.3.1 Time temperature transformation curves

During isothermal heat treatments, supersaturated aluminum matrix would decompose to form precipitates, leading to the change of electrical resistivity of the samples. The evolution of the electrical conductivity of solution treated Aural™-5 HPVD samples at different isothermal temperatures shown in fig. 4.21 (a). At first stage, the electrical conductivity increases rapidly and then the

increasing rate decreases gradually, and finally, the electrical conductivity reaches a stable stage as the extension of isothermal time. At 350°C, the increasing rate of the electrical conductivity is the fastest, for example, it reaches 42 % IACS in 400s. However, at lower or higher temperature the electrical conductivity increases with a much low rate. The electrical conductivity of solution treated sample is 38.5% IACS, which represents the supersaturated solid solution state. The conductivity of isothermal holding at 350°C for 27h is 43.50% IACS, which represents complete decomposition of supersaturated solid solution. The time-temperature transformation (TTT) curves were constructed using the values of 10%, 20% and 40% of the difference of the electrical conductivity between the supersaturated and the complete decomposition samples as shown in fig. 4.21 (b). Nose temperature, quench sensitivity temperature range and critical time at nose temperature in the TTT curves are generally accepted to be the prime factors in determining the quench sensitivity. The nose temperature of Aural^{TM}-5 HPVD is 350°C, and the quench sensitivity temperature range is 260-430°C. Electrical conductivity changes rapidly in the sensitivity temperature range with the extension of isothermal time. The critical time for 10% precipitate transformation is 16s.

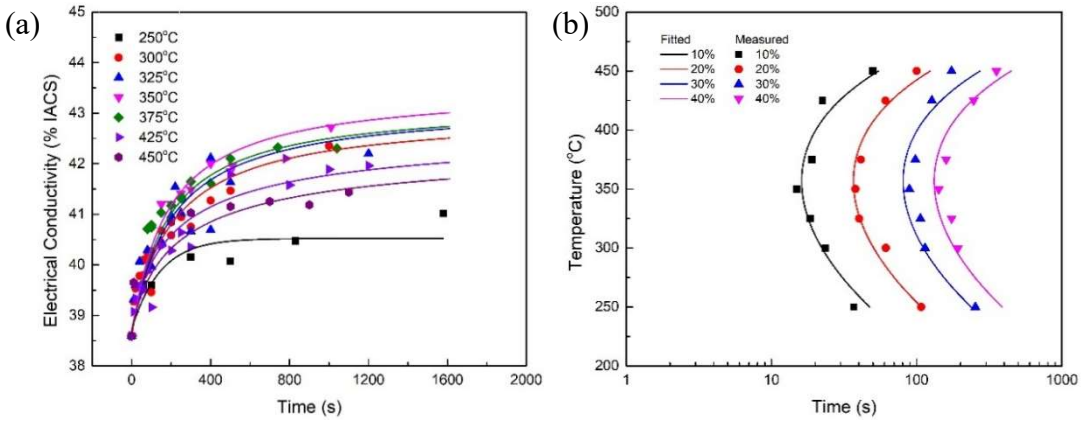

Figure 4.21: the electrical conductivity evolution as function of isothermal temperature and holding time (a); TTT curves of Aural^{TM}-5 HPVD samples (b).

4.3.2 Time temperature property curves

The hardness of Aural^{TM}-5 HPVD castings on T6 condition (500°C for 3 hours followed by 170°C for 2.5 hours) is 73.3HV0.1. But, it decreases with the extension of the holding time at isothermal temperatures. Figure 4.22 (a) illustrates the evolution of hardness of solution treated Aural^{TM}-5 HPVD samples as the functions of isothermal temperatures and holding time. Generally, the hardness decreases rapidly at first stage, then the decrease rate significantly slows with the extension of the time. At moderate temperature, 350°C, the decrease rate is fastest, reaching 58HV0.1 in 200s. However, at lower or higher temperature the hardness decreases at a much low rate.

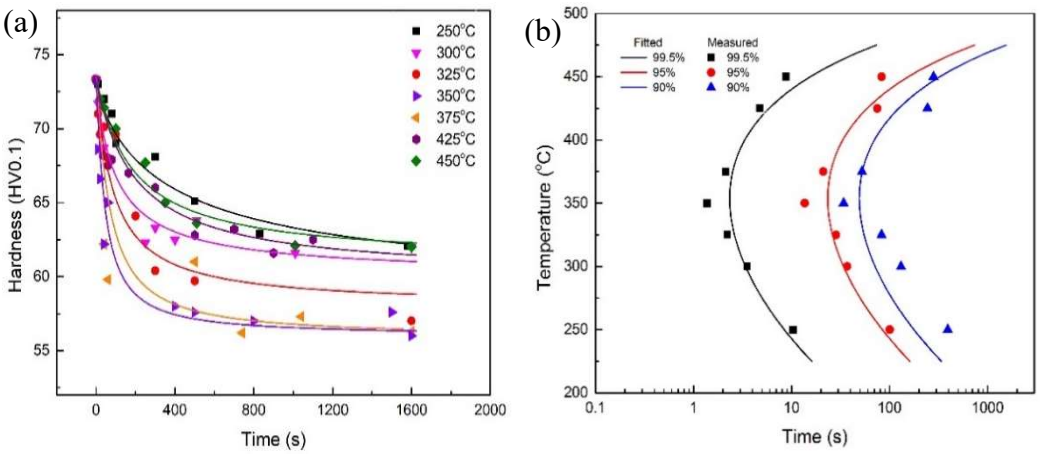

Figure 4.22: (a) hardness evolution as function of isothermal temperatures and holding time; (b) TTP curve of Aural™-3 HPVD samples.

Table 4.5 : Coefficients for TTP diagram of Aural™ 5 and Aural™ 3 HPVD.

Castings	k2	k3 (J/mol)	k4(K)	k5(J/mol)
A5-HPVD	2.38×10^{-6}	2866	945	74247
A3-HPVD	1.92×10^{-6}	2483	955	72966

Table 4.5 showed the coefficients in the equation determined by non-linear least squares that was obtained when the hardness data is applied to Eq. (2.3).

The TTP curves with values of 99.5%, 95%, 90%, and 80% of the maximum property performance of Aural™ 5 HPVD samples, are shown in figure 2.22 (b), respectively. The TTP curves posse "C" shape. The nose temperature is 350°C. The quench sensitivity temperature range is around 260-430 °C, in which, 0.5% of hardness drop is less than 10 seconds. The hardness decreasing rate in the temperature range is much higher than that outside of this temperature range. The critical time at nose temperature is 2.4s to obtain 99.5% maximum hardness.

4.3.3 Quench factor analysis

Figure 4.23 (a) illustrates the relationship of cooling rate, quench factor and hardness based on TTP curves and Eqs. (4.2, 4.3 and 4.4). As cooling rate increases, quench factor falls rapidly, at first stage, then the decrease of the quench factor becomes slowly. Conversely, hardness initially rapidly increases with the increase of cooling rate, then the increase smooth out. Figure 4.23(b) demonstrates the relationship between cooling rate and hardness drop. When the cooling rate is 6 ºC/s or higher than 6 ºC/s, the hardness drop is 5% or less than 5%. On the other words, if the cooling rate is higher than 6 ºC/s, more than 95% of maximum mechanical performance of the samples would be obtained. Here, the cooling rate to reach 95% of maximum mechanical performance is referred to as critical quench rate, C_r. The dark line represents predicted data based on quench factor analysis, and the red dots represent measured data obtained from experiment samples. The predicted results are agreed to experimental measured data well.

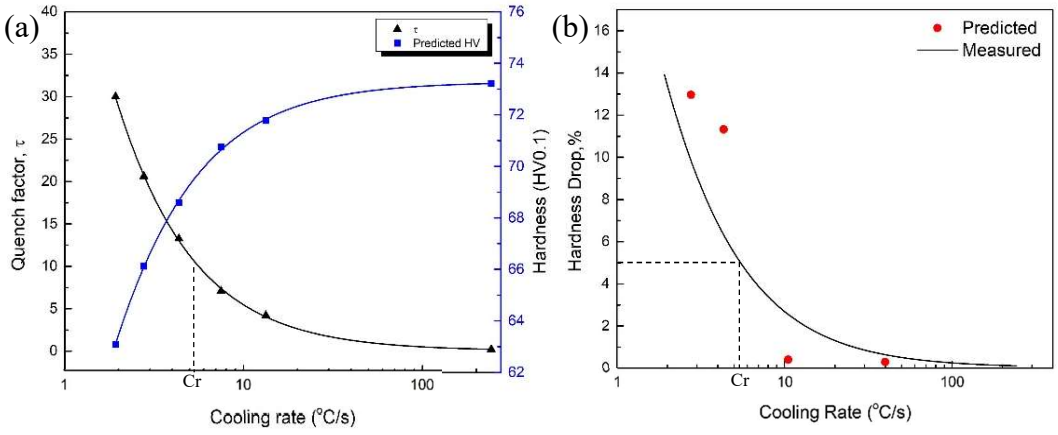

Figure 4.23: (a) Effect of average cooling rate on quench factor and predicted hardness of Aural™ 5 HPVD alloy (b)drop in property vs. quenching rate of Aural™ 5 HPVD.

4.3.4 Avrami kinetics

Avrami kinetics equation, $\psi = 1 - \exp(-kt^n)$, is generally applied to describe the kinetics of phase transformation, where ψ is the volume fraction of the precipitation at the time *t*; *k* is the Avrami constant depending on the nucleation rate and the growth rate, and very sensitive to temperature; *n* is the Avrami exponent which is depending on the nucleation mechanism[56, 57]. The precipitated volume fraction ψ at the time t can be got from the TTP curves (the marks in figure 4.24). By using Avrami equation to do the iterative non-linear fitting procedure, we can obtain the time-dependent volume fraction of the precipitation as function of different temperatures, as illustrated in figure 4. The Avrami parameters are shown in table 4.6. A large value of *k* in Avrami kinetics equation is relative to a high phase transformation rate[38, 58]. According to Table 4.6, nose temperature of TTP and TTT, 350 ºC, has the highest *k* value, which indicates the fastest transformation occurred at this temperature. At higher or lower temperature, the transformation rates gradually decrease. The transformation reaction process is slow during the first 50s transformation period at 350ºC, after which the rate increased rapidly. At other temperatures, it follows the similar tendency, but the time for the phase transformation is longer.

There are two types of precipitation mechanisms in phase transformation, one is diffusion-controlled process, and the other one is nucleation-controlled process [38, 56]. The former occurs at the temperature lower than the nose temperature while the latter occurs at the temperature higher than the nose temperature. For diffusion-controlled precipitation, when the value of Avrami

exponent *n* is approximately 1, it indicates that precipitates have the morphologies of thickening of long cylinder or needle-like shapes. But, when *n* = 1 for nucleation-controlled precipitation, it means that the precipitates are mainly formed at grain boundary[38, 56]. Therefore, according to the values of *n* in table 3, the needle-like precipitates would present in Aural™-5 when the phase transformation at a temperature lower than nose temperature, and if the phase transformation occurs at a temperature higher than nose temperature, the precipices would form along grain boundaries.

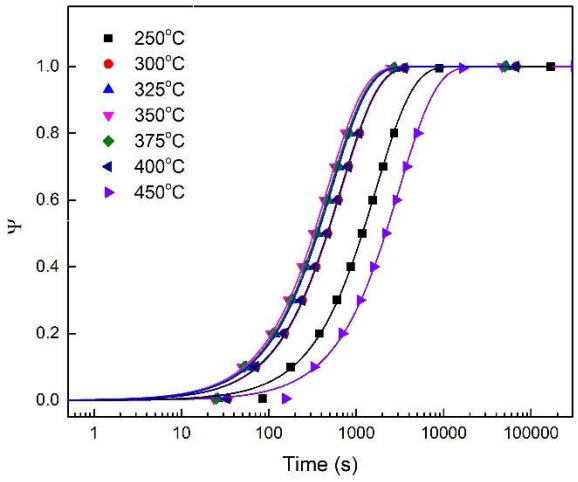

Figure 4.24 : Precipitate transformation as function of holding time during isothermal treatment for Aural™-5 HPVD samples.

Table 4.6 : Avrami parameters of Aural™ 5 HPVD alloy.

Casting		250°C	300°C	325°C	350°C	375°C	400°C	450°C
Aural™5	k	0.0005	0.0013	0.0017	0.0019	0.0017	0.0013	0.0003
	n	1.0233	1.0230	1.0230	1.0228	1.0229	1.0226	1.0236

4.3.5 Microstructure analysis

Figure 4.25 (a) is the optical microstructure of Aural^{TM}-5 HPVD samples on T4 (500 ºC 3h) condition. The microstructure of the HPVD sample is consist of α-Al phase, spherized Si phase particles, Fe-rich intermetallic phase, and a small amount of Mg_2Si. Figure 4.25(b) is EBSD mapping image of the samples. The average grain diameter is around 10.3μm, and the length of grain boundary per square micrometers is 6.2 μm. It means that there is a lot of grain boundaries in the HPVD samples, which will be benefit for the precipitation on grain boundaries.

Figure 4.26 shows the TEM images of the isothermal treated samples at 350ºC, nose temperature, for 300s. A small amount of Mg_2Si with length of 0.5-1 μm are observed in aluminum matrix as shown in figure 4.26 (a), while there is a large number of granular Mg_2Si line up at grain boundary as shown in figure 4.26 (b). On the other side, for the T6 treated sample (500 ºC for 3h, plus 170 ºC for 2.5h), as shown in figure 4.27, we can see a high density of fine needle-like Mg_2Si precipitates of 50−200 nm in length in the matrix. Therefore, the property variation of the HPVD samples at different heat treatment conditions is attributed to the different types of Mg_2Si phase precipitation during the treatment process. Moreover, it is the evident of the Avrami kinetics that when the isothermal treatment at the temperature lower than the nose temperature, the needle-like precipitates distribute in aluminum matrix, but when the precipitation is controlled by nucleation and diffusion-controlled mechanisms at nose temperature, the precipitates nucleate along grain boundaries and matrix.

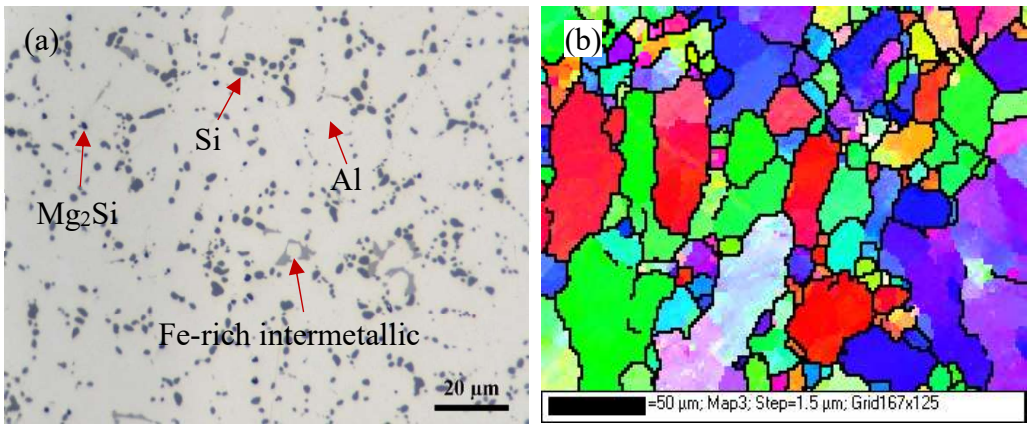

Figure 4.25 : (a) optical microscope image of Aural™ 5 HPVD 500℃3h sample (b) EBSD mapping images of Aural™ 5 HPVD 500℃ 3h sample.

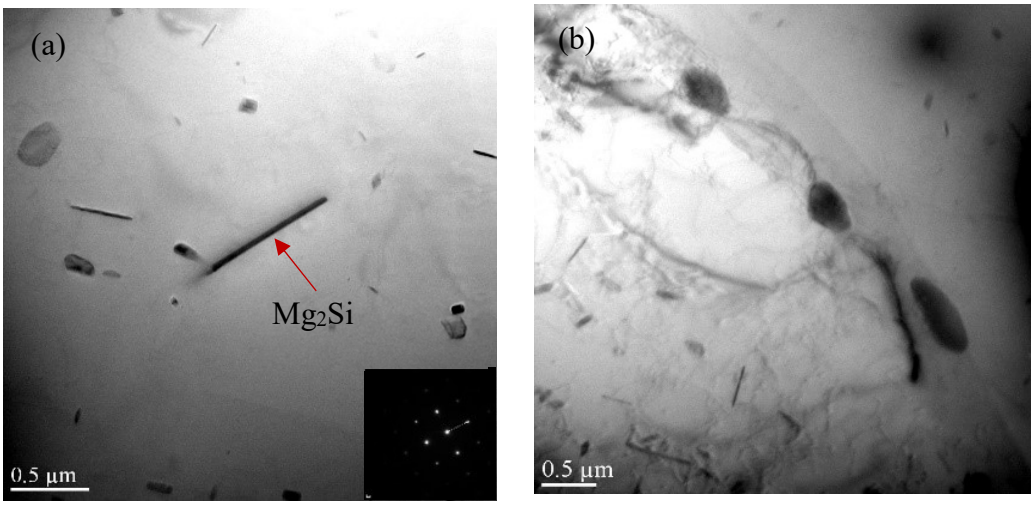

Figure 4.26 : TEM images (a) Aural™ 5 HPVD as-quenched sample at 350℃ 300s with SAD pattern at $[001]_{\alpha\text{-Al}}$ direction (b) grain boundary of Aural™ 5 HPVD as-quenched sample at 350℃ 300s.

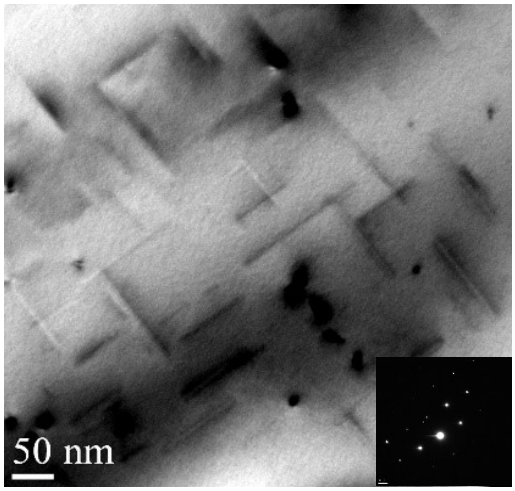

Figure 4.27 : TEM image of A5 HPVD as-aged specimen with the SAD pattern at $[001]_{\alpha\text{-Al}}$ direction.

4.3.6 Comparison of quench sensitivity of Aural™ 5 and Aural™ 3 HPVD castings

Chapter 4.2 investigated the effect of casting processes on quench sensitivity of Aural™ 3 alloy, they found that the HPVD had higher quench sensitivity than PM due to fine grain size which was caused by high solidification rate. For the purpose of comparison, 99.5% of maximum hardness of Aural™ 3 HPVD and Aural™ 5 HPVD were selected, as shown in figure 4.28. Table 4.7 listed the parameters of quench sensitivity for Aural™ 3 and 5 HPVD. Aural™ 5 HPVD has lower nose temperature and longer critical time at nose temperature than Aural™ 3, but the broad of quench sensitivity temperature range of Aural™ 5 HPVD is the same as that of Aural™ 3 HPVD. A much slower cooling rate, 6℃/s, was required for Aural™ 5 to maintain 95% of maximum hardness, while it is 20℃/s for Aural™ 3 HPVD to achieve the same level of hardness. All these parameters indicate that Aural™ 5 HPVD has lower quench sensitivity than Aural™ 3 HPVD.

The low quench sensitivity is mainly due to the different concentration of Mg and Si in the two alloys. Excessive Si content would precipitate during quenching, acted as nucleation sites, and increase quench sensitivity[36]. Both alloys have excessive Si content, meaning Mg content is the main factor determining quench sensitivity. The addition of increased amounts of Mg (0.2%Mg in Aural™-5, 0.55%Mg in Aural™-3) results in a large increase in solute supersaturation in the matrix, with a consequential increase in the driving force of precipitations during aging. Additionally, high driving force will lead to

a rise in precipitation nose temperatures[28]. On the other side, Aural™-3 HPVD possesses a lower value of k_3, and higher k_4 than Aural™-5 HPVD. The former is the constant corresponding to the energy for a nucleus formation and the latter is corresponding to Mg_2Si solvus temperature in TTP curves (see Figs. 2.2 and 2.3, Table 4.5). All of these factors imply the nucleation in Aural™-3 HPVD is easier and faster than that in Aural™-5 HPVD.

According to Table 4.8, the length of the grain boundary in Aural™ 3 is around twice of Aural™ 5 HPVD, which means that Aural™ 3 HPVD would provide more nucleation sites in grain boundaries than Aural™ 5 HPVD. This can also be confirmed by the k_2, constant associated with the reciprocal of the number of nucleation sites, shown in Table 4.5. Aural™ 3 has a lower value of k_2 than Aural™ 5. Moreover, the grain boundaries provide fast solute diffusion passages, which would be in benefit the precipitate nucleation and growth. It is also demonstrated by the k_5, corresponding to diffusion energy values. The value of k_5 in Aural™-3 HPVD is lower than that in Aural™-5 HPVD.

Therefore, Aural™-5 HPVD has less nucleation sites, lower nucleation driving force, higher energy requested for nucleus formation than Aural™-3 HPVD. Consequently, Aural™-5 HPVD has lower quench sensitivity than Aural™ 3 HPVD.

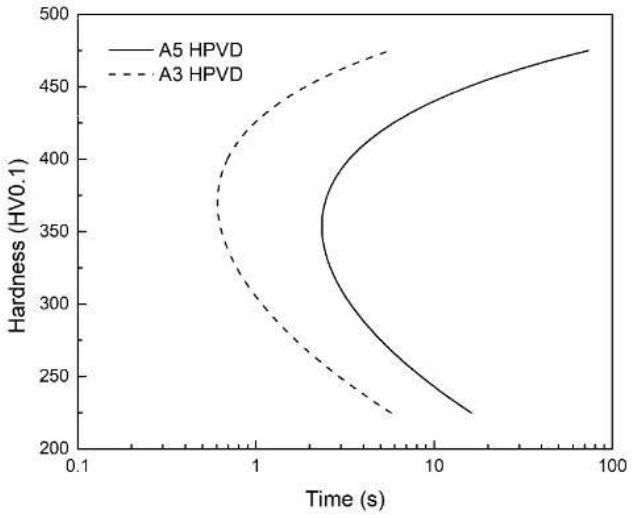

Figure 4.28 : TTP curves of 99.5% max hardness of Aural™ 5 HPVD (solid) and Aural™ 3 HPVD (dash).

Table 4.7 : Parameters of quench sensitivity of Aural™-3/5 HPVD.

Castings	Nose T	Sensitivity T range	Critical time at nose T of 99.5% TTP curves	Quench rate for 5% hardness drop
Aural™ 5	350 °C	250-430 °C	2.4s	6 °C/s
Aural™ 3	375 °C	270-450 °C	0.6s	20 °C/s

Table 4.8 : Grain size (equivalent diameter) and grain boundaries in HPVD.

	Grain diameter (μm)		Grain boundary length per μm^2 ($\mu m/\mu m^2$)	
Castings	Average	STD	Average	STD
Aural™ 5	10.3	6.1	6.3	0.2
Aural™ 3	4.4	3.5	11.3	0.7

4.3.7 Summary

1. The time-temperature-transformation (TTT) curves and time-temperature-precipitation (TTP) curves of Aural^{TM} 5 HPVD castings have been determined. The nose temperature of TTT and TTP curves is 350ºC. The quench sensitivity temperature range of TTT and TTP is 260-430 ºC. At nose temperature, the phase transformation rate is the fastest.

2. The effect of cooling rates on mechanical properties were established using quench factor analysis method. The cooling rate should be higher than 6ºC/s to obtain higher than 95% of maximum mechanical performance. The predicted results are agreed to the experimental measured data well.

3. Mg_2Si precipitation causes the variation of mechanical performance of Aural^{TM}-5 HPVD samples during heat treatment. When heat treatment at 170ºC, needle-like Mg_2Si precipitates distribute in aluminum matrix. But when treated at nose temperature, the precipitates are mainly located along grain boundaries.

4. Aural^{TM}-5 HPVD has lower quench sensitivity than Aural^{TM}-3 HPVD.

Chapter 5 Conclusion and suggestions for further work

5.1 Conclusions

The main conclusions could be summarized as follow:

1. In the high pressure vacuum die (HPVD) casting, there exists a surface layer which can be divided into 1) a skin sublayer directly adjacent to the cast surface, 2) a eutectic-rich sublayer next to the skin sublayer and followed by 3) an aluminum grain-rich sublayer. There is a significant macrosegregation of Si and Mg in the HPVD samples. It is enriched in the surface layer and depleted in the center of the sample, which also affected the mechanical properties. The macrosegregation is not obvious in PM samples.

2. Aural^{TM} 3 HPVD alloy has a higher quench sensitivity than Aural^{TM} 5 HPVD and Aural^{TM} 3 PM, as indicated by the fact that it has the highest nose temperature, and shortest critical time. In order to maintain 95% of the maximum hardness, Aural^{TM} 3 HPVD needed a cooling rate over 20^{o}C/s, which is higher than Aural^{TM} 3 PM (17^{o}C/s) and Aural^{TM} 5 HPVD (6^{o}C/s).

3. The casting process influences the microstructures which have an effect on precipitation behavior and a resultant impact on quench sensitivity. High solidification rates in HPVD produce fine grain sizes. At nose temperature we are more likely to see Mg_2Si precipitates mainly locate along grain boundaries. For PM, Mg_2Si is more likely to be observed at the matrix due to the presence of large grain size and Mn-containing dispersoids in the aluminum matrix.

4. Chemical composition has a great impact on quench sensitivity. Aural^{TM} 5 has a lower content of Si and Mg than Aural^{TM} 3, which reduces the degree of supersaturation and leads to a lower driving force for precipitation. Meanwhile, the grain boundary precipitation in Aural^{TM} 5 HPVD is not as strong as that in Aural^{TM} 3 HPVD, because the grain boundaries in Aural^{TM} 5 HPVD is less than that in Aural^{TM} 3 HPVD.

5.2 Suggestions for further work

The study concentrated on the effect of casting processes and chemical compositions on quench sensitivity of Al-Si-Mg alloys. Based on the results obtained in this research. It would be useful to investigate the following concepts:

1. To analyze the interrelation of grain size or the length of grain boundary and quench sensitivity of Al-Si-Mg alloys.

2. To explore the relationship of grain size or the length of grain boundary and quench sensitivity of other alloys.

3. To investigate the link between the parameters of TTT and parameters of TTP.

Reference

1. Tinto, R., *Aluminium Your guide to automotive innovation.* 2016: p. 12, 13.
2. Ji, S., et al., *Microstructural evolution and solidification behavior of Al-Mg-Si alloy in high-pressure die casting.* Metallurgical and Materials Transactions A, 2013. **44**(7): p. 3185-3197.
3. Gourlay, C., H. Laukli, and A. Dahle, *Defect band characteristics in Mg-Al and Al-Si high-pressure die castings.* Metallurgical and Materials Transactions A, 2007. **38**(8): p. 1833-1844.
4. Wang, L.-Y., Zheng, L.-S., Qu,W.-T., Zhou, X.-C., Xu, J.-W. , *Special casting processes.* Industry Press, Beijing, China, 1984: p. 196.
5. Hamasaiid, A., et al., *Effect of mold coating materials and thickness on heat transfer in permanent mold casting of aluminum alloys.* Metallurgical and materials Transactions A, 2007. **38**(6): p. 1303-1316.
6. Lee, F., J. Major, and F. Samuel, *Effect of silicon particles on the fatigue crack growth characteristics of Al-12 Wt Pct Si-0.35 Wt Pct Mg-(0 to 0.02) Wt Pct Sr casting alloys.* Metallurgical and Materials Transactions A, 1995. **26**(6): p. 1553-1570.
7. Hoskin, G., J. Provan, and J. Gruzleski, *The in-situ fatigue testing of a cast aluminum-silicon alloy.* Theoretical and applied fracture mechanics, 1988. **10**(1): p. 27-41.
8. Osório, W.R., P.R. Goulart, and A. Garcia, *Effect of silicon content on microstructure and electrochemical behavior of hypoeutectic Al–Si alloys.* Materials Letters, 2008. **62**(3): p. 365-369.
9. Caceres, C., et al., *The effect of Mg on the microstructure and mechanical behavior of Al-Si-Mg casting alloys.* Metallurgical and Materials Transactions A, 1999. **30**(10): p. 2611-2618.
10. Ouellet, P. and F. Samuel, *Effect of Mg on the ageing behaviour of Al-Si-Cu 319 type aluminium casting alloys.* Journal of Materials Science, 1999. **34**(19): p. 4671-4697.
11. Li, Y. and L. Arnberg, *Quantitative study on the precipitation behavior of dispersoids in DC-cast AA3003 alloy during heating and homogenization.* Acta Materialia, 2003. **51**(12): p. 3415-3428.
12. Kashyap, K., et al., *Casting and heat treatment variables of Al–7Si–Mg alloy.* Materials science and technology, 1993. **9**(3): p. 189-204.
13. Lim, C. and H.R. Shercliff, *Quench sensitivity of aluminium alloy 6082.* 1993.
14. Evancho, J. and J. Staley, *Kinetics of precipitation in aluminum alloys during continuous cooling.* Metallurgical Transactions, 1974. **5**(1): p. 43.
15. Staley, J., *Quench factor analysis of aluminium alloys.* Materials Science and Technology, 1987. **3**(11): p. 923-935.
16. Ives, L.K., et al., *The NBS: Processing/Microstructure/Property Relationships in 2024 Aluminum Alloy Plates.* 1983.
17. Okayasu, M., et al., *A study of the mechanical properties of an Al–Si–Cu alloy (ADC12) produced by various casting processes.* Materials Science and Engineering: A, 2012. **543**: p. 185-192.

18. Tiryakioğlu, M. and R.T. Shuey, *Quench sensitivity of an Al-7 Pct Si-0.6 Pct Mg alloy: characterization and modeling.* Metallurgical and Materials Transactions B, 2007. **38**(4): p. 575-582.
19. Zhang, D. and L. Zheng, *The quench sensitivity of cast Al-7 wt pct Si-0.4 wt pct Mg alloy.* Metallurgical and Materials Transactions A, 1996. **27**(12): p. 3983-3991.
20. Gruzleski, J.E. and B.M. Closset, *The treatment of liquid aluminum-silicon alloys*. 1990: Amer Foundry Society.
21. Belov, V.S.Z.a.N.I., *Casting Aluminum Alloys,.* Elsevier, Amsterdam, The Netherlands, 2007.
22. Backerud, L., G. Chai, and J. Tamminen, *Solidification characteristics of aluminum alloys. Vol. 2. Foundry alloys.* American Foundrymen's Society, Inc., 1990, 1990: p. 266.
23. Heusler, L. and W. Schneider, *Recent Investigations of Influence of P on Na and Sr Modification of Al-Si Alloys (97-97).* Transactions of the American Foundrymen's Society, 1997. **105**: p. 915-922.
24. Hess, P. and E. Blackmun, *Strontium as a modifying agent for hypoeutectic aluminum-silicon alloys.* Paper from" Transactions of the Americal Foundrymen's Society., 1975. **83**.
25. Fourmann, F.B.a.J., *Alloys with high strength and ductility for high pressure vacuum die casting in automotive body structure applications: impact of heat treatment on mechanical properties.* Die Casting Congress & Tabletop conference, 2016.
26. MacKenzie, G.E.T.a.D.S., *Handbook of Aluminum: Vol. 1: Physical Metallurgy and Processes.* CRC press, 2003.
27. Ma, S., et al., *A methodology to predict the effects of quench rates on mechanical properties of cast aluminum alloys.* Metallurgical and Materials Transactions B, 2007. **38**(4): p. 583-589.
28. Chaudhury, S.K. and D. Apelian, *Effects of Mg and Cu Content on Quench Sensitivity of Al–Si–Mg Alloy.* International Journal of Metalcasting, 2016. **10**(2): p. 138-146.
29. Rometscht, P. and G. Schaffer, *Quench modelling of Al-7Si-Mg casting alloys.* International Journal of Cast Metals Research, 2000. **12**(6): p. 431-439.
30. *Casting metals.* Open university.
31. Todd, R.H., D.K. Allen, and L. Alting, *Manufacturing processes reference guide*. 1994: Industrial Press Inc.
32. DeGarmo, E.P., J. Black, and R.A. Kohser, *Materials and processes in manufacturing, 1997*. Prentice-Hall, Englewood Cliffs, New Jersey.
33. Street, A., *The Die Casting Books.* Portcullis Press Ltd., 1977: p. 625-641.
34. Kendall, K., A. Howard, and J.D. Birchall, *The relation between porosity, microstructure and strength, and the approach to advanced cement-based materials.* Phil. Trans. R. Soc. Lond. A, 1983. **310**(1511): p. 139-153.
35. Lee, S., et al., *Effect of process parameters on porosity distributions in high-pressure die-cast AM50 Mg-alloy.* Materials Science and Engineering: A, 2006. **427**(1-2): p. 99-111.
36. Niu, X.P., et al., *Vacuum assisted high pressure die casting of aluminium alloys.* Journal of Materials Processing Technology, 2000. **105**(1): p. 119-127.

37. Fatahalla, N., M. Hafiz, and M. Abdulkhalek, *Effect of microstructure on the mechanical properties and fracture of commercial hypoeutectic Al-Si alloy modified with Na, Sb and Sr.* Journal of Materials Science, 1999. **34**(14): p. 3555-3564.
38. Porter, D.A., K.E. Easterling, and M. Sherif, *Phase Transformations in Metals and Alloys, (Revised Reprint)*. 2009: CRC press.
39. Mohamed, A. and F. Samuel, *A review on the heat treatment of Al-Si-Cu/Mg casting alloys*, in *Heat Treatment-Conventional and Novel Applications*. 2012, InTech.
40. Abdel-Jaber, G., et al., *An investigation into solidification and mechanical properties behavior of Al-Si casting alloys.* International Journal of Mechanical & Mechatronics Engineering IJMME-IJENS, 2010. **10**(1).
41. Kim, H.Y., et al., *Effects of Mn on the crystal structure of α-Al (Mn, Fe) Si particles in A356 alloys.* Journal of Crystal Growth, 2006. **291**(1): p. 207-211.
42. Rana, R., R. Purohit, and S. Das, *Reviews on the influences of alloying elements on the microstructure and mechanical properties of aluminum alloys and aluminum alloy composites.* International Journal of Scientific and Research Publications, 2012. **2**(6): p. 1-7.
43. Robinson, M., *: B.A.Sc. Thesis.* University of Queensland, Queensland, 1996.
44. Zhong, H., et al., *The influence of Mg/Si ratio and Cu content on the stretch formability of 6xxx aluminium alloys.* Materials Science and Engineering: A, 2016. **651**: p. 688-697.
45. Abedi, K. and M. Emamy, *The effect of Fe, Mn and Sr on the microstructure and tensile properties of A356–10% SiC composite.* Materials Science and Engineering: A, 2010. **527**(16-17): p. 3733-3740.
46. Hu, R., et al., *Dispersoid formation and recrystallization behavior in an Al-Mg-Si-Mn alloy.* Journal of Materials Science & Technology, 2010. **26**(3): p. 237-243.
47. Rometsch, P., et al. *The effect of homogenizing on the quench sensitivity of 6082*. in *Materials Science Forum*. 2002. Trans Tech Publ.
48. Robson, J., *Microstructural evolution in aluminium alloy 7050 during processing.* Materials Science and Engineering: A, 2004. **382**(1-2): p. 112-121.
49. Association, A., *Aluminum: properties and physical metallurgy*. 1984: ASM International.
50. Ferguson, J. and Z. Kemblowski, *Applied fluid rheology*. 1991: Springer.
51. Totten, G., G. Webster, and C. Bates, *Quench factor analysis: step-by-step procedures for experimental determination.* The first international non-ferrous processing and technology conference., 1997: p. 305-13.
52. Liu, S.-d., et al., *TTP curve of 7055 aluminum alloy and its application.* Chinese Journal of Nonferrous Metals, 2006. **16**(12): p. 2034.
53. Dutta, I. and S. Allen, *A calorimetric study of precipitation in commercial aluminium alloy 6061.* Journal of Materials Science Letters, 1991. **10**(6): p. 323-326.
54. Andersen, S., et al., *The crystal structure of the β ″phase in Al–Mg–Si alloys.* Acta Materialia, 1998. **46**(9): p. 3283-3298.

55. Du, Y., et al., *Diffusion coefficients of some solutes in fcc and liquid Al: critical evaluation and correlation.* Materials Science and Engineering: A, 2003. **363**(1-2): p. 140-151.
56. Avrami, M., *Kinetics of phase change. I General theory.* The Journal of chemical physics, 1939. **7**(12): p. 1103-1112.
57. Christian, J.W., *The theory of transformations in metals and alloys*. 2002: Newnes.
58. Li, S.-l., et al., *Quench sensitivity of 6351 aluminum alloy.* Transactions of Nonferrous Metals Society of China, 2013. **23**(1): p. 46-52.